Shigella IpaA mediates actin bundling through diffusible vinculin oligomers with activation imprint

Cesar Valencia-Gallardo, Daniel-Isui Aguilar-Salvador, Hamed Khakzad, Benjamin Cocom-Chan, Charles Bou-Nader, Christophe Velours, Yosra Zarrouk, Christophe Le Clainche, Christian Malosse, Diogo Borges Lima, et al.

Cell Reports

Article

Shigella IpaA mediates actin bundling through diffusible vinculin oligomers with activation imprint

Graphical abstract

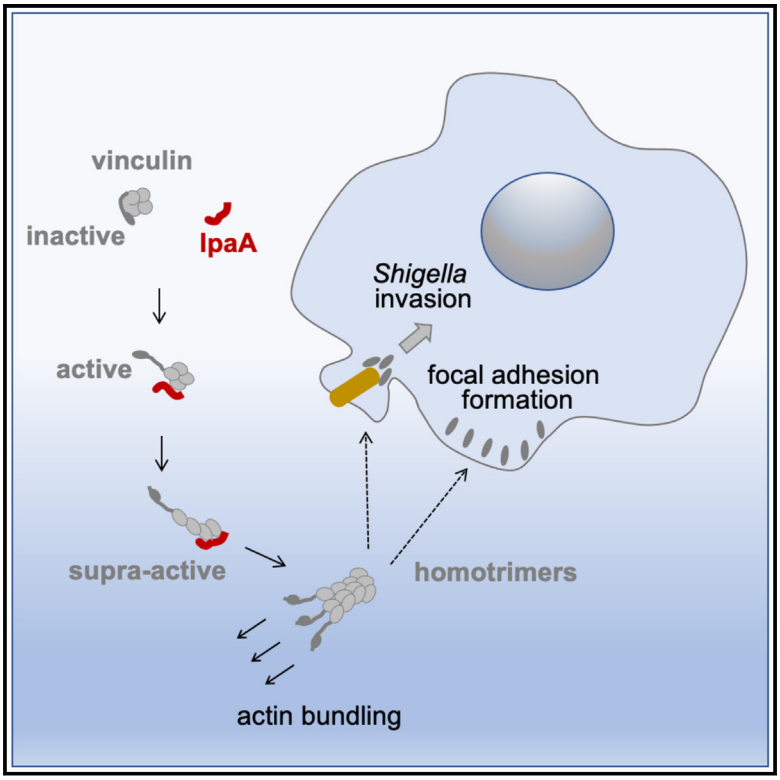

Highlights

- *Shigella* IpaA induces vinculin oligomerization via the D1D2 head subdomains
- IpaA-induced vinculin oligomers promote actin bundling
- IpaA stimulates the formation of highly stable focal adhesions
- Focal adhesions triggered by IpaA form independent of acto-myosin contraction

Authors

Cesar Valencia-Gallardo, Daniel-Isui Aguilar-Salvador, Hamed Khakzad, ..., Julia Chamot-Rooke, Lars Malmström, Guy Tran Van Nhieu

Correspondence

guy.tranvannhieu@i2bc.paris-saclay.fr

In brief

Valencia-Gallardo et al. show that the *Shigella* invasion effector IpaA induces major conformational changes in the vinculin head domain leading to vinculin oligomerization and actin filament bundling. This non-canonical mode of vinculin activation is required for bacterial invasion and may also be pertinent for the formation of cell adhesion structures.

Valencia-Gallardo et al., 2023, Cell Reports *42*, 112405
April 25, 2023
https://doi.org/10.1016/j.celrep.2023.112405

CellPress

Cell Reports

CellPress
OPEN ACCESS

Article

Shigella IpaA mediates actin bundling through diffusible vinculin oligomers with activation imprint

Cesar Valencia-Gallardo,[1,11] Daniel-Isui Aguilar-Salvador,[1,2,11] Hamed Khakzad,[1,2,12] Benjamin Cocom-Chan,[1,2,3,12] Charles Bou-Nader,[4,12] Christophe Velours,[5] Yosra Zarrouk,[3] Christophe Le Clainche,[6] Christian Malosse,[7] Diogo Borges Lima,[7] Nicole Quenech'Du,[1] Bilal Mazhar,[1] Sami Essid,[2] Marc Fontecave,[4] Atef Asnacios,[8] Julia Chamot-Rooke,[7] Lars Malmström,[9] and Guy Tran Van Nhieu[1,2,3,10,13,*]

[1]Center for Interdisciplinary Research in Biology (CIRB), Team "Ca^{2+} Signaling and Microbial Infections," Collège de France, CNRS UMR7241/INSERM U1050, PSL Research University, 75005 Paris, France

[2]Laboratoire de biologie et Pharmacie Appliquée (LBPA), CNRS UMR8113/INSERM U1282, Team "Ca^{2+} Signaling and Microbial Infections," Ecole Normale Supérieure Paris-Saclay, Université Paris Saclay, 91190 Gif-sur-Yvette, France

[3]Institute for Integrative Biology of the Cell (I2BC), CNRS UMR9198/INSERM U1280, Team "Ca^{2+} Signaling and Microbial Infections," CEA, Université Paris-Saclay, 91190 Gif-sur-Yvette, France

[4]Laboratoire de Chimie des Processus Biologiques, Collège De France, CNRS UMR8229, 75005 Paris, France

[5]Fundamental Microbiology and Pathogenicity Laboratory, UMR 5234 CNRS-University of Bordeaux, SFR TransBioMed, 33076 Bordeaux, France

[6]Institute for Integrative Biology of the Cell (I2BC), CNRS UMR9198, Team "Cytoskeletal Dynamics and Motility", CEA, Université Paris-Saclay, 91190 Gif-sur-Yvette, France

[7]Institut Pasteur, Université Paris Cité, CNRS UAR 2024, Mass Spectrometry for Biology Unit, F-75015 Paris

[8]Université Paris Cité, CNRS, Laboratoire Matière et Systèmes Complexes, UMR7057, F-75013 Paris, France

[9]Division of Infection Medicine, Department of Clinical Sciences, Lund University, Lund, Sweden

[10]Present address: I2BC, CNRS UMR 9198/INSERM U1282, 91190 Gif-sur-Yvette, France

[11]These authors contributed equally

[12]These authors contributed equally

[13]Lead contact

*Correspondence: guy.tranvannhieu@i2bc.paris-saclay.fr

https://doi.org/10.1016/j.celrep.2023.112405

SUMMARY

Upon activation, vinculin reinforces cytoskeletal anchorage during cell adhesion. Activating ligands classically disrupt intramolecular interactions between the vinculin head and tail domains that bind to actin filaments. Here, we show that *Shigella* IpaA triggers major allosteric changes in the head domain, leading to vinculin homo-oligomerization. Through the cooperative binding of its three vinculin-binding sites (VBSs), IpaA induces a striking reorientation of the D1 and D2 head subdomains associated with vinculin oligomerization. IpaA thus acts as a catalyst producing vinculin clusters that bundle actin at a distance from the activation site and trigger the formation of highly stable adhesions resisting the action of actin relaxing drugs. Unlike canonical activation, vinculin homo-oligomers induced by IpaA appear to keep a persistent imprint of the activated state in addition to their bundling activity, accounting for stable cell adhesion independent of force transduction and relevant to bacterial invasion.

INTRODUCTION

Shigella, the causative agent of bacillary dysentery, invades epithelial cells by injecting type III effectors that locally reorganize the actin cytoskeleton.[1–3] *Shigella* invasion involves limited contacts with host cells and critically depends on the type III effector IpaA that promotes cytoskeletal anchorage by targeting the focal adhesion (FA) proteins talin and vinculin.[2,4,5] During integrin-mediated cell adhesion, talin acts as a mechanosensor by exposing its vinculin-binding sites (VBSs) that recruit and activate vinculin, reinforcing anchorage to the actin cytoskeleton in response to mechanical load.[6–8] Because of its small mass and size, *Shigella* cannot generate the type of mechanical load required for strong cytoskeletal anchorage; therefore, scaffolding of talin and vinculin at bacterial invasion sites exclusively relies on IpaA. IpaA contains three VBSs in its C-terminal moiety, with diverse functions inferred from the crystal structures of complexes containing the VBS peptide.[9,10] Vinculin is classically described as a head domain connected to a tail domain by a flexible linker.[11] The vinculin head contains three repetitions (D1–D3) of a conserved domain consisting of two antiparallel α-helix bundles and a fourth α-helix bundle, D4.[11] A proline-rich

unstructured linker bridges D4 and a five-helix bundle vinculin tail containing the C-terminal F-actin-binding domain.[11] Under its inactive folded form, intramolecular interactions between the vinculin head and tail prevent ligand binding. IpaA VBS1, as for all VBSs described to activate vinculin, interacts with the first helical bundle of the D1 domain, promoting major conformational changes that disrupt the head-tail intramolecular interactions and free the vinculin F-actin-binding region.[12] IpaA VBS2, in contrast, interacts with the second helical bundle of D1[10]; hence, its association with IpaA VBS1 results in a very high affinity and stable IpaA VBS1–2:D1 complex, with an estimated K_D in the femtoM range.[10] Functional evidence indicates that IpaA VBS3 cooperates with IpaA VBS1–2 to stimulate bacterial invasion.[5,13] IpaA VBS3, as an isolated peptide, acts as IpaA VBS1 by interacting with the vinculin D1 first helical bundle and promotes vinculin activation.[13] IpaA VBS3, however, can also interact with talin to stimulate bacterial capture by filopodia during the early *Shigella* invasion phase of host cells.[5] The structural data indicate that IpaA VBS3 stabilizes the H1-H4 helix bundle expected to form in a partially stretched talin conformer at the low force range exerted by filopodia.[5] Intriguingly, IpaA VBS3 shares with talin VBS10 (H46) the ability to bind to vinculin and talin H1H4, suggesting a complex interplay between talin and vinculin during mechanotransduction.[5] Unlike talin VBSs, IpaA VBSs are not buried into helix bundles, presumably enabling targeting of vinculin and talin in a serendipitous manner.

In addition to strengthening cytoskeletal anchorage, vinculin has also been implicated in the bundling of actin filaments through dimerization via its tail domain, triggered by F-actin or phosphatidylinositol(4, 5) bisphosphate (PIP2) binding.[14–16] Consistent with a key role in vinculin tail-mediated actin bundling, mutations in the vinculin tail that prevent PIP2 binding lead to defects in FA dynamics and formation.[16] Also, mutations that prevent vinculin tail dimerization or alter C-terminal hairpin involved in actin bundling lead to defects in FA formation and cell spreading, although the correlation between F-actin bundling activity and the amplitude of adhesion defects is unclear.[17] The role of vinculin tail-induced dimerization in scaffolding, however, remains unclear since it cannot simply explain the formation of high-order complexes. The formation of these high-order vinculin complexes could implicate the recruitment of other vinculin-binding partners or vinculin oligomerization mechanisms other than through vinculin tail, possibly through vinculin head-head interactions observed in the so-called "parachute" structures.[18] Of interest, upon activation, vinculin is known to promote the scaffolding of adhesion components during FA growth and maturation, a process that may also implicate its oligomerization.[19] More recently, through its interaction with branched actin networks and the bundling activity of talin-vinculin scaffolds, vinculin was also proposed to regulate the dynamics of actin polymerization at adhesion structures.[20] These studies also pointed to the observation that vinculin-mediated actin bundling occurred at the site of vinculin activation,[20] thereby imposing a frame spatially limiting the actin bundling activity of vinculin during adhesion maturation.

Here, we investigated the role of vinculin at the cell cortical sites of *Shigella* invasion, where all three IpaA VBSs are expected to bind target vinculin.[5] We show that the combined action of IpaA VBSs induces major conformational changes in the vinculin head domain, a process that we coined "supra-activation." These changes lead to the formation of vinculin homo-oligomers, promoting the bundling of actin filaments at a distance from the activation site. Our results suggest that vinculin supra-activation also occurs during mechanotransduction and is required for maturation of cell adhesions.

RESULTS

IpaA VBS1–3 is required for full recruitment of vinculin at *Shigella* contact sites

IpaA VBS3 targets a partially unfolded talin conformer, during early bacterial capture by filopodia, but is not expected to bind to fully activated talin.[5] Instead, at higher force ranges associated with FA maturation at the cell cortex, IpaA VBS3 is expected to target vinculin in combination with IpaA VBS1 and -2. To test this, we analyzed adhesion structures induced by *Shigella* during bacterial invasion.

As shown in Figure 1A and as previously reported,[9] *Shigella* triggers the IpaA-dependent recruitment of vinculin at phagocytic cups (Figures 1A, arrows, and 1B, wild type [WT]). Vinculin recruitment was strongly reduced at bacterial contact sites induced by the *ipaA* mutant complemented with IpaA ΔVBS1–2 expressing only IpaA VBS3[13] (Figures 1A, 1B, ΔVBS1–2, and S1). IpaA ΔVBS1–2 triggered the recruitment of small vinculin patches, but large phagocytic cups as observed for the WT strain were not detected (Figures 1A, arrows, and 1B). We previously identified mutations A495K and K498E in IpaA VBS3 affecting talin, but not vinculin, binding.[5] We found that these mutations did not affect the recruitment of vinculin small patches triggered by IpaA ΔVBS1–2, consistent with a direct role of IpaA VBS3 in vinculin binding at bacterial contact sites (Figures 1A, 1B, A495K and K498E, and S1). Consistent with previous talin staining results, IpaA also induced the formation of vinculin-containing FAs distal to bacterial invasion sites[5] (Figure 1A, arrowheads). In contrast to bacterial contact sites, these distal FAs formed at similar extents for WT *Shigella* and *ipaA*/IpaA ΔVBS1–2 but were affected in talin-binding-deficient VBS3 derivatives (Figures 1A, arrowheads, 1C, and S1), suggesting that vinculin recruitment at distal FAs occurred indirectly through talin.

These results indicate that IpaA VBS3 binding to vinculin is required for the full recruitment of this cytoskeletal linker at phagocytic cups during *Shigella* invasion. In contrast, IpaA VBS3 appears to play a distinct role in bacterial-induced distal FAs, for which its talin-binding property is critical, while vinculin binding is dispensable. These findings point at different functions of IpaA VBS3, contrasting with a mere role in vinculin scaffolding during *Shigella* invasion.

IpaA induces vinculin higher-order oligomerization

Previous analytical size-exclusion chromatography (SEC) studies suggested that IpaA can bind to multiple vinculin molecules through its three VBSs.[13] In the proposed model and akin to the model proposed for talin VBSs during mechanotransduction, each IpaA VBS binds to one vinculin molecule through interaction via the first bundle of the vinculin D1 subdomain,

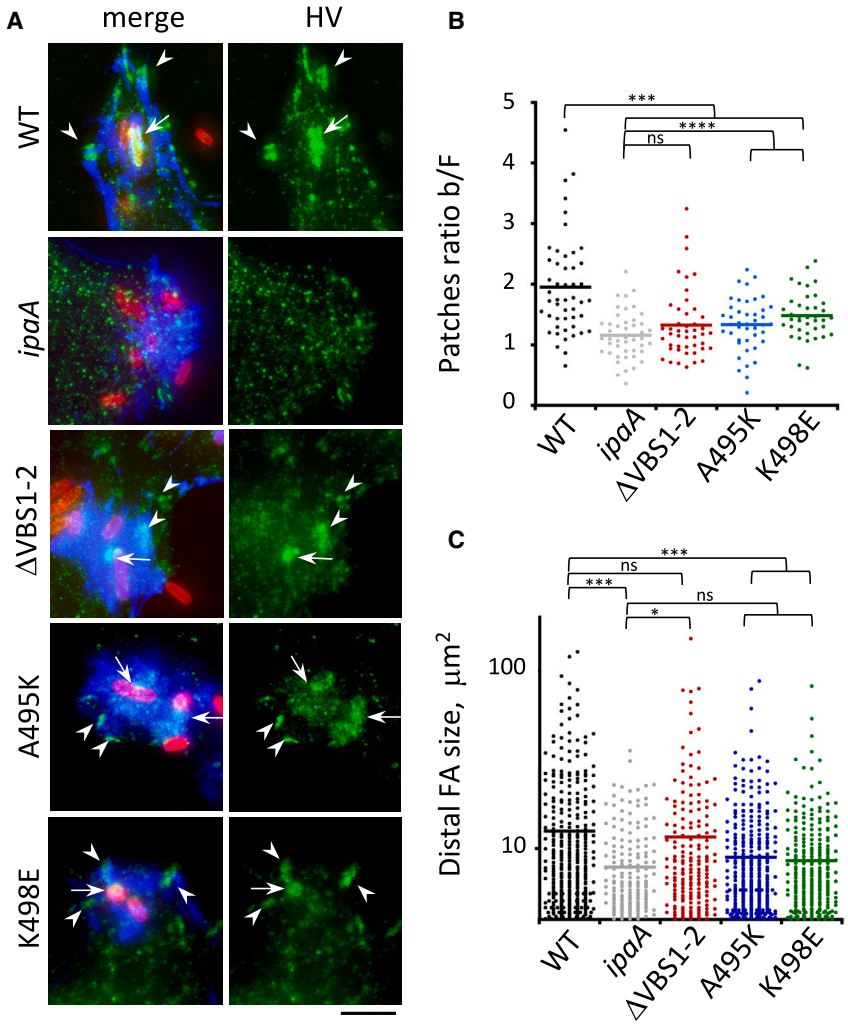

Figure 1. Vinculin recruitment at *Shigella* contact sites and distal adhesion structures during bacterial invasion

HeLa cells were challenged with bacteria for 30 min at 37°C, fixed, and processed for immunofluorescence staining. *ipaA* mutant complemented with full-length IpaA (WT), control vector (*ipaA*), IpaA ΔVBS1–2 (ΔVBS1–2), IpaAΔVBS1–2 A495K (A495K), and IpaAΔVBS1–2 K498E (K498E).

(A) Representative micrographs. Merge: maximum projection of deconvolved confocal planes. Vinculin: confocal plane corresponding to the cell basal surface. Red: bacteria; green: vinculin; blue: F-actin. Vinculin recruitment at bacterial contact sites (arrows) and distal adhesion structures (arrowheads). Scale bar: 5 µm.

(B) Vinculin recruitment at bacterial contact sites was quantified as the ratio of average fluorescence intensity of vinculin labeling associated with the bacterial body over that of actin foci (STAR Methods; Figure S1). The average ratio ± SEM is indicated. WT: 1.94 ± 0.11 (48 foci, N = 2); *ipaA*: 1.15 ± 0.05 (46 foci, N = 2); ΔVBS1–2: 1.32 ± 0.08 (45 foci, N = 2); A495K: 1.33 ± 0.07 (42 foci, N = 2); K498E: 1.48 ± 0.06 (38 foci, N = 2).

(C) Large vinculin adhesion structures were scored as detailed in the STAR Methods. Average FA size ± SEM µm^2: WT: 12.54 ± 0.76 (393 FAs, N = 2); *ipaA*: 8.48 ± 0.49 (201 FAs, N = 2); ΔVBS1–2: 11.59 ± 1.08 (207 FAs, N = 2); A495K: 8.96 ± 0.45 (376 FAs, N = 2); K498E: 8.56 ± 0.44 (291 FAs, N = 2). Mann and Whitney test: *p < 0.05; ***p < 0.005; ****p < 0.001.

leading to its activation (Figure 2A).[13] This view supports a redundant role for IpaA VBSs inconsistent with a differential role of IpaA VBS3 suggested in the previous set of experiments.

To further characterize the role of IpaA VBS3 on vinculin binding, we studied the effects of the IpaA derivatives containing VBS1–2 (AVBS1–2) or VBS1–3 (AVBS1–3) on binding to derivatives containing different subdomains of the vinculin head (D1–D4) using SEC-MALS (multiangle light scattering) (Figure 2B). When analyzing binding of AVBS1–3 to the D1 first subdomain of vinculin corresponding to residues 1–257 and consistent with previous SEC results,[13] AVBS1–3:D1 complexes with a molar ration of 1:1, 2:1, and 3:1 were observed, likely corresponding to the scaffolding of D1 molecules on the 3 IpaA VBSs based on the predicted molecular mass of the complexes (Figure 2C). We then analyzed complexes formed upon incubation of AVBS1–3 with a construct containing vinculin residues 1–834 (D1D4), corresponding to full-length human vinculin (HV) devoid of the C-terminal F-actin-binding domain (Figure 2B). As shown in Figure 2D, we found 1:1 D1D4:AVBS1–3, but unexpectedly, complexes containing 2 and 3 D1D4 molecules were also observed (Figure 2D). Similar complexes containing 2 and 3 molecules of a derivative containing only the vinculin residues 1–484 (Figure 2F, D1D2) were seen upon incubation with AVBS1–3, indicating that vinculin oligomerization only required the vinculin D1 and D2 subdomains. By contrast, when AVBS1–2 were incubated with D1D2, 1:1 and 2:0–2:1 D1D2:AVBS1–2 complexes were detected, but no D1D2 trimers (Figure 2E). Because of the small size of AVBS1–2 and AVBS1–3 and the low extinction coefficient difference between complex partners, the detection limits of the SEC-MALS equipment did not allow us to unambiguously distinguish between 2:0 and 2:1 D1D2:AVBS1–2 or 3:0 and 3:1 D1D2:AVBS1–3 complexes. However, the discrepancy between the determined and expected molecular masses of the complexes, as well as the slopes observed for the molecular mass, argued that the peak corresponded to 2:0 and 2:1 or 3:0 and 3:1 complexes in equilibrium (Figures 2D–2F). In line with this, quantitative SDS-PAGE analysis of the peak fractions indicated a molar ratio comprised between 2:0 and 2:1 and between 3:0 and 3:1 for D1D2:AVBS1–2 and D1D2:AVBS1–3, respectively, consistent with a mixture of interexchanging complexes present in the corresponding peaks (Figure S2).

These results suggest that binding of IpaA VBS1–3 to vinculin triggers conformational changes leading to the formation of vinculin trimers.

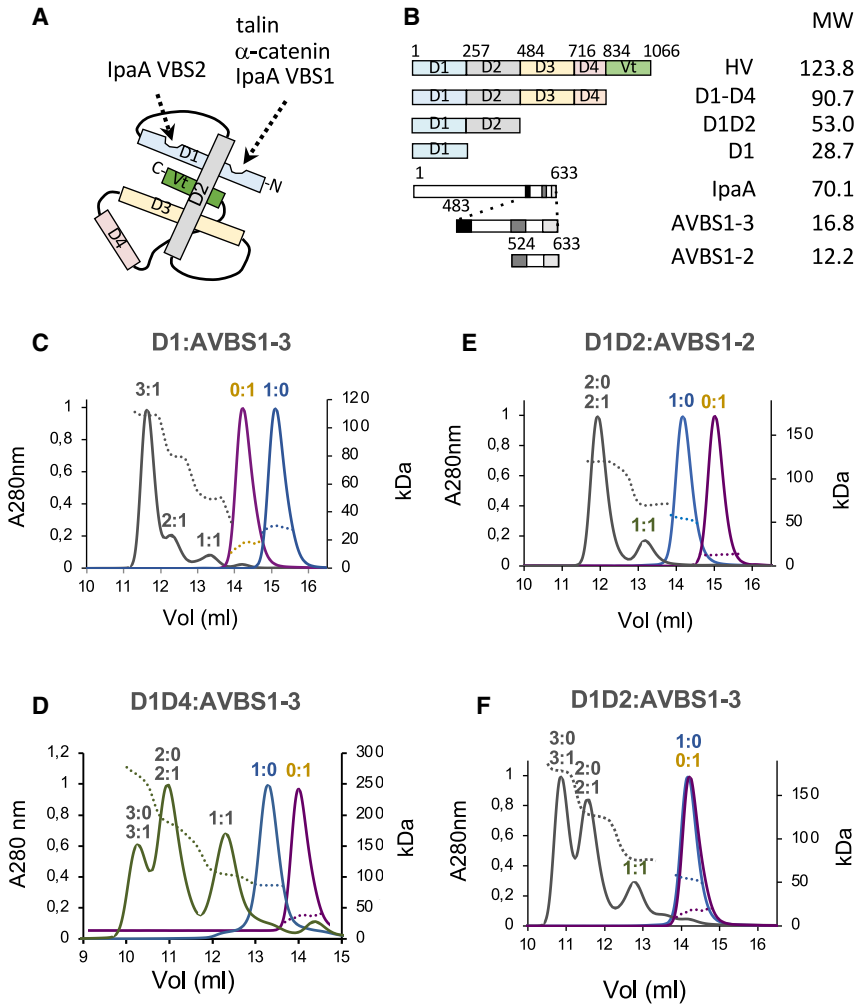

Figure 2. IpaA promotes vinculin homo-oligomerization

(A) Scheme of folded vinculin (HV). The binding sites and corresponding ligands are indicated.

(B) Scheme of vinculin and IpaA constructs. Vinculin domains and IpaA VBSs are depicted as boxes. The numbers indicate the start residue of each domain. MW: molecular weight in kDa.

(C–F) SEC elution profiles of complexes formed shown as follows. Green trace: between AVBS1–3 (C, D, and F) or AVBS1–2 (E) and the indicated vinculin derivatives; blue trace: the indicated vinculin derivative alone; purple trace: AVBS1–2 (E) or AVBS1–3 alone (C, D, and F). The indicated complex stoichiometry was inferred from the molecular weight estimated by MALS. Dotted line: molecular weight.

IpaA promotes major conformational changes in the vinculin D1 D2 domains

To further investigate mechanism responsible for vinculin oligomerization, we performed binding assays with vinculin derivatives immobilized onto a solid phase to restrict conformational changes. By constraining conformation of vinculin derivatives, we expected to prevent the formation of higher-order oligomers observed in solution while enabling binding of IpaA VBSs to initial sites on the vinculin derivative conformers. These assays indicated that AVBS1–3 and AVBS1–2 bound to vinculin with a similar affinity as estimated in Figure S3A by their EC50 (95% confidence interval) of 6.1 (4.2–9) and 3.7 (1.7–8.1) nM, respectively. Strikingly, a large difference was observed in the binding plateau, indicating that vinculin presented more binding sites for AVBS1–3 than for AVBS1–2 (Figure S3A). D1D2 presented more binding sites than the D1 domain only, suggesting the presence of additional sites on the D2 domain (Figure S3B). Consistently, BN-PAGE showed the formation of 1:1, as well as a 1:2, D1D2:AVBS1–3 complexes, observed with an increasing AVBS1–3 M ratio (Figure S3C). In contrast, single 1:1 complexes were observed for D1:AVBS1–3, D1:AVBS1–2, or D1D2:AVBS1–2 (Figures S3C–S3H), indicating that IpaA VBS3 was required to reveal additional sites on the D2 domain. These results suggested that as for immobilization on solid phase, the presence of Coomassie brilliant blue in BN-PAGE interfered with higher-order vinculin oligomerization while enabling binding to the vinculin derivative monomer. Together, these results suggested that the formation of vinculin oligomers triggered by AVBS1–3 required the IpaA VBS3-dependent exposure of binding sites on D2. These findings were unexpected since vinculin activating ligands have been described to bind to a single site on the D1 domain of vinculin.

To map interactions between AVBS1–2 and AVBS1–3 with D1D2, complexes were cross-linked, subjected to proteolysis, and analyzed using liquid chromatography coupled to mass spectrometry (LC-MS) (STAR Methods). Intermolecular links were identified from the characterization of cross-linked peptides and, along with identified intramolecular links, used to produce structural models (Tables S1–S3; Figures S4A and S4B; STAR Methods). The D1:AVBS1–2 complex showed links consistent with a "canonical" conformer expected from established structures[2,9] (Figure S4C). Similar links were identified for the D1D2:AVBS1–2 complex, with a majority of links observed with the D1 domain (Figure S4D). For both complexes, the structure shows interactions between IpaA VBS1 and VBS2 with the D1 first and second bundles, respectively, leading to helical bundle reorganization of D1 associated with vinculin activation[12] (Figures S4C and S4D). For the D1D2:AVBS1–3 complex, MS-based structural modeling reveals two major conformers accounting for the majority of links. In a first "closed" conformer, IpaA VBS1 and VBS2 interact with the D1 bundles in a similar manner as for AVBS1–2, where the relative positioning of D1 and D2 is globally conserved compared with apo D1D2 or the D1D2:AVBS1–2 complex (Figures 3A, S4D, and S4E). In this closed conformer, IpaA VBS3 interacts with an interface formed by the H5 (residues 128–149) and H8 (residues 222–250) helices in the second bundle of D1 and the H13

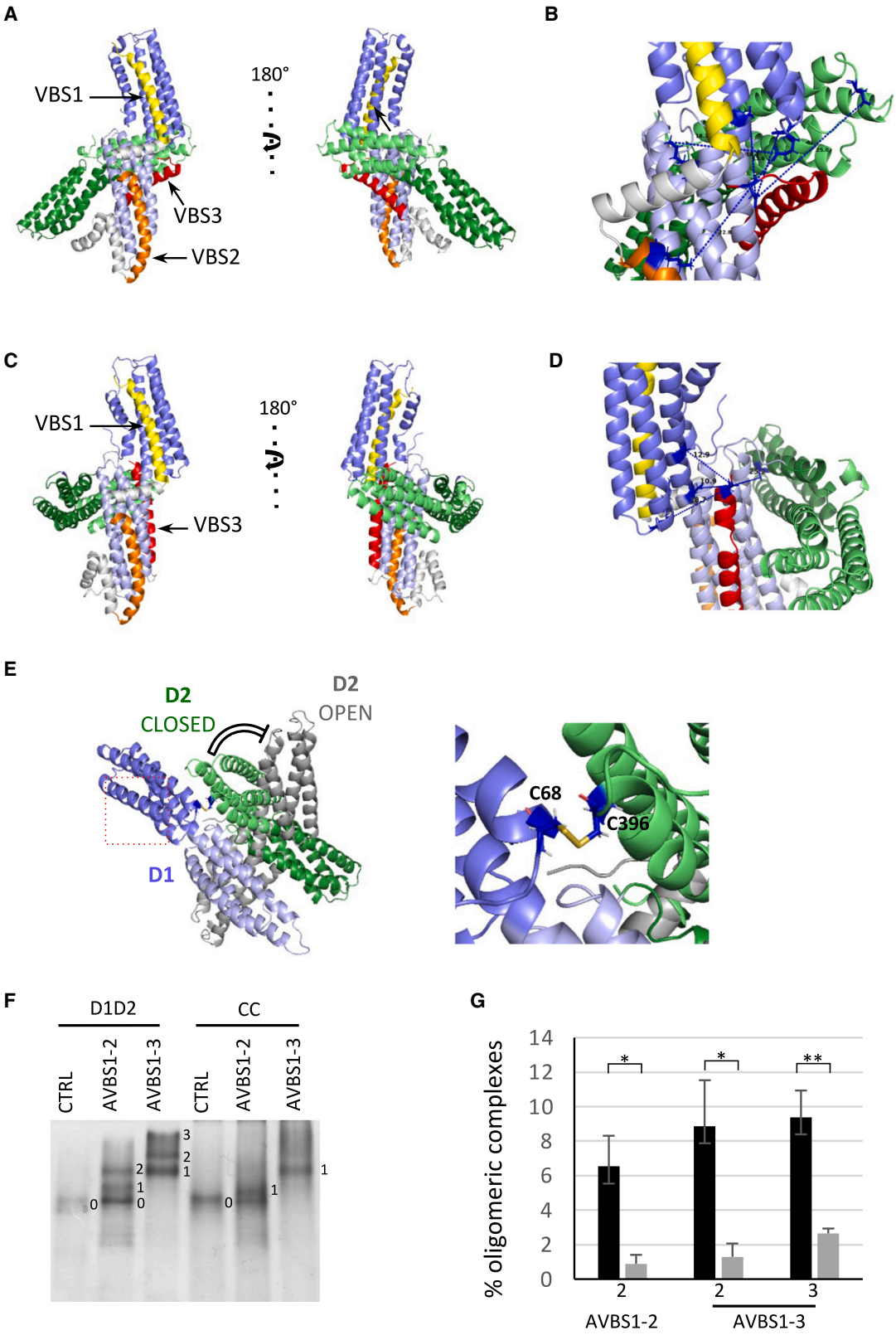

(legend on next page)

(residues 373–397) helix in the second bundle of D2 (Figures 3A and 3B). The second open conformer, however, shows a major reorientation of D1 and D2 subdomains, with their major axis forming an angle value of ca. 82° compared with the 25° observed in the native vinculin structure or the first conformer, with IpaA VBS3 docking sidewise through extensive interactions with the H5 (residues 128–149) and H8 (residues 222–250) helices of D1 (Figures 3C and 3D, light blue helices). Since this latter conformer was observed for AVBS1–3 but not for AVBS1–2, we posited that it was involved in the formation of higher-order D1D2 complexes and homo-trimers. To test this, we engineered mutations substituting residue Q68 in the first D1 bundle and A396 in the second D2 bundle for cysteine residues, expected to prevent the formation of the open conformer upon disulfide bridge formation (Figure 3E) by preventing major conformational shifts of the D1 and D2 domains. In control experiments, disulfide bridge formation was detected in D1D2 and full-length HV containing the Q68C and A396C mutations, expected to act as a clamp preventing the major conformational changes induced by AVBS1–3 (Figures S5A–S5C).

As shown in Figure 3F, two and three upper-shifted D1D2 bands were visualized by clear native PAGE upon incubation with AVBS1–2 and AVBS1–3, respectively. Quantitative second-dimension SDS-PAGE analysis of the upper-shifted bands 2 and 3 upon incubation with AVBS1–3 indicated a D1D2: AVBS1–3 M ratio superior to 3, suggesting that these likely corresponded to the 2:0–2:1 and 3:0–3:1 higher-order D1D2 complexes observed in the SEC-MALS analysis (Figures 2, S2, and S5E), although with a different representativity perhaps linked to electrophoretic conditions. The cysteine clamp Q68C A396C (CC) in D1D2 did not prevent the exposure of additional sites on D2 or 1:1 complex formation induced by AVBS1–2 or AVBS1–3. However, CC prevented the formation of higher-order complexes for D1D2 as well as for full-length vinculin (Figures 3F and S5F. HV-CC). In control experiments, as opposed to the double Q68C A396C substitutions, the single Q68C and A396C substitutions did not prevent D1D2 oligomer formation in native gel shift assays (Figures S6A and S6B). We coined "supra-activation" the mode of vinculin activation induced by AVBS1–3 involving major conformational changes in the vinculin head to distinguish it from the canonical activation associated with the dissociation of vinculin head-tail domains.

IpaA mediates actin bundling and vinculin-talin co-clusters

To further characterize the role of vinculin supra-activation, we performed actin co-sedimentation assays. As expected, the cysteine clamp had little effect on vinculin canonical activation since the majority of cysteine-clamped full-length vinculin (HV-CC) associated with actin filaments upon incubation with AVBS1–2 or AVBS1–3 (Figures S7A and S7B). We then tested the ability of vinculin oligomers to promote actin bundling by performing low-speed sedimentation assays (STAR Methods). As shown in Figure 4, vinculin alone did not promote actin bundling (Figures 4A and 4B, HV). Upon incubation with AVBS1–3, up to 30% of the total actin pool sedimented, consistent with AVBS1–3-mediated vinculin actin bundling. This actin bundling activity was associated with the low-speed co-sedimentation of vinculin with actin (Figure 4A). In contrast, no such actin bundling activity was observed for HV-CC even upon incubation with AVBS1–3 (Figures 4A and 4B). Together, these results suggest that vinculin oligomers triggered by IpaA-mediated vinculin supra-activation can bundle actin filaments.

Next, we asked how vinculin oligomers promoted actin bundling relative to the site of AVBS1–3-mediated supra-activation. Indeed, vinculin homo-oligomers are not expected to remain bound to AVBS1–3 but to diffuse away from activation sites. To test this, we designed a solid-phase assay where GST-AVBS1–3 was coated on 1 μM diameter fluorescent beads (STAR Methods). Control experiments indicated that GST-AVBS1–3 showed little desorption from beads up to 2 h following coating (Figures S7C and S7D). HV was fluorescently labeled and incubated with GST-AVBS1–3-coated beads in actin polymerization assays (STAR Methods). As shown in Figure 4C, vinculin clusters were clearly detected in association with actin bundles, away from AVBS1–3-coated beads. As expected, such vinculin clusters were observed to a much lesser extent with beads coated with AVBS1–2, control GST, and the HV-CC cysteine clamp construct (Figures 4C and 4D). Also, consistent with low-speed actin sedimentation results, actin bundling was prominent upon incubation with AVBS1–3-coated beads, relative to AVBS1–2- and GST-coated beads, and was not observed for HV-CC (Figures 4C and 4D). These results are consistent with the formation of vinculin homo-oligomers induced by AVBS1–3-mediated supra-activation, bundling actin filaments away from the activation sites.

Figure 3. IpaA promotes major conformational changes in the vinculin D1 D2 domains

(A–E) Structural models of D1D2-IpaA VBS1–3. Pale blue: D1 first bundle. Dark blue: D1 second bundle. Pale green: D2 first bundle. Dark green: D2 second bundle. Yellow: IpaA VBS1. Orange: IpaA VBS2. Red: IpaA VBS3.

(A and B) "Closed" conformer.

(C and D) "Open" conformer.

(B and D) Higher magnification of the IpaA VBS3-D1D2 interaction in (A) and (C) showing the identified cross-linked distance between residues in Å. IpaA VBS1–3 were docked on the surface of vinculin D1D2 and verified using MS cross-link constraints. Targeted cross-linking (TX)-MS protocol[21] in combination with MS constraints was used to unify and adjust the final model, which justifies over 100 cross-links.

(E) Structural model of cysteine-clamped vinculin. Green: D2 in the closed conformer. Gray: D2 domain in the open conformer. Black: C68-C396 cysteine clamp preventing the switch from closed to open conformers. Right panel: enlarged view of the cysteine clamp shown in the inset in the left panel.

(F) Native gel analysis of vinculin D1D2 and IpaA derivatives. D1D2 or the double cysteine mutant D1D2 (CC) were incubated with the indicated IpaA derivatives and analyzed by native PAGE followed by Coomassie staining. The numbers next to the band indicate upper-shifted bands of D1D2:AVBS1–2 or D1D2:AVBS1–3 complexes. Note the absence of higher-order complexes for the CC mutant.

(G) The band integrated intensities corresponding to the indicated shifted bands were quantified using ImageJ. Values are expressed as the percentage of total protein amounts in the corresponding sample. Solid bars: D1D2. Gray bars: CC. N = 3. Error bar, SEM. t-test, *$p < 0.05$; **$p < 0.01$.

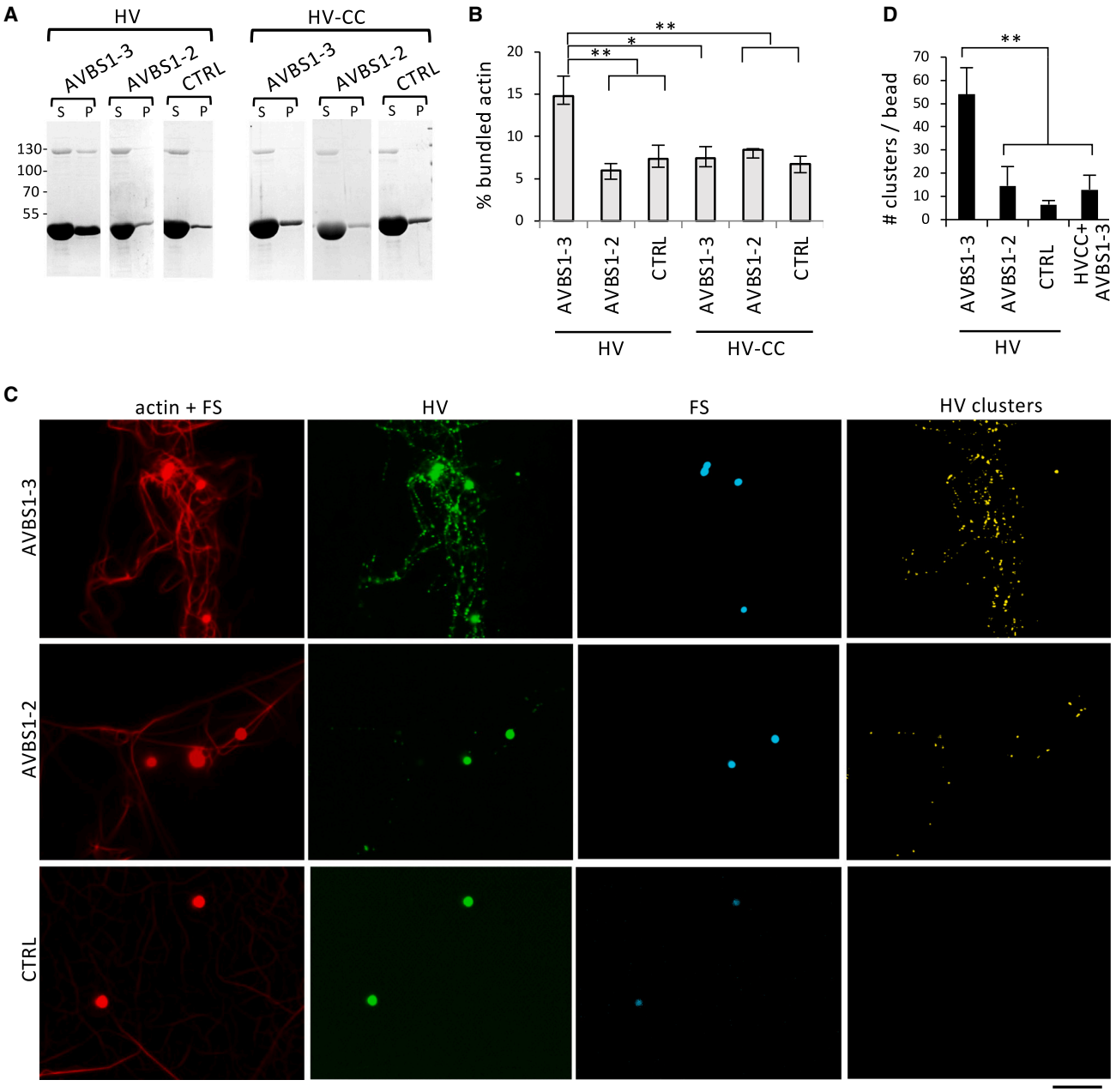

Figure 4. IpaA-induced vinculin oligomers promote actin bundling

(A and B) Actin sedimentation assays. HV: full-length human vinculin; HV-CC: cysteine-clamp derivative. Actin was allowed to polymerize at a final concentration of 20–30 μM in the presence of the indicated proteins. Samples were centrifuged at 14,000 × *g* for 10 min to pellet actin bundles, respectively.

(A) Representative SDS-PAGE analysis using a 10% polyacrylamide gel followed by Coomassie staining. S, supernatant; P, pellet.

(B) The band integrated intensity corresponding to actin was quantified using ImageJ. Values are expressed as the percentage of actin in the pellet fraction relative to the total actin amounts in the supernatant and pellet fractions normalized to control. Percentage of bundled actin; HV (n = 9, N = 4); HV-CC (n = 6, N = 3). N = 3. Error bar, SEM. t-test, *p < 0.05; **p < 0.01.

(C) Representative micrographs of fluorescently labeled actin polymerized in the presence of Bodipy-vinculin and coated beads. Beads were coated with AVBS1–3, AVBS1–2, or GST (control [CTRL]). Red: actin; green: Bodipy-vinculin; cyan: beads; yellow: detected HV clusters (see STAR Methods). Numerous vinculin clusters are observed at a distance from AVBS1–3 coated beads.

(D) The numbers of vinculin clusters per bead ± SEM are shown for the indicated samples (N = 3, HV+AVBS1–3: 1292; N = 2, HV+AVBS1–2: 120; N = 2, HV+GST (CTRL): 56; N = 2, HVCC+AVBS1–3: 80). Scale bar: 5 μm. Mann and Whitney. *p < 0.05; **p < 0.01.

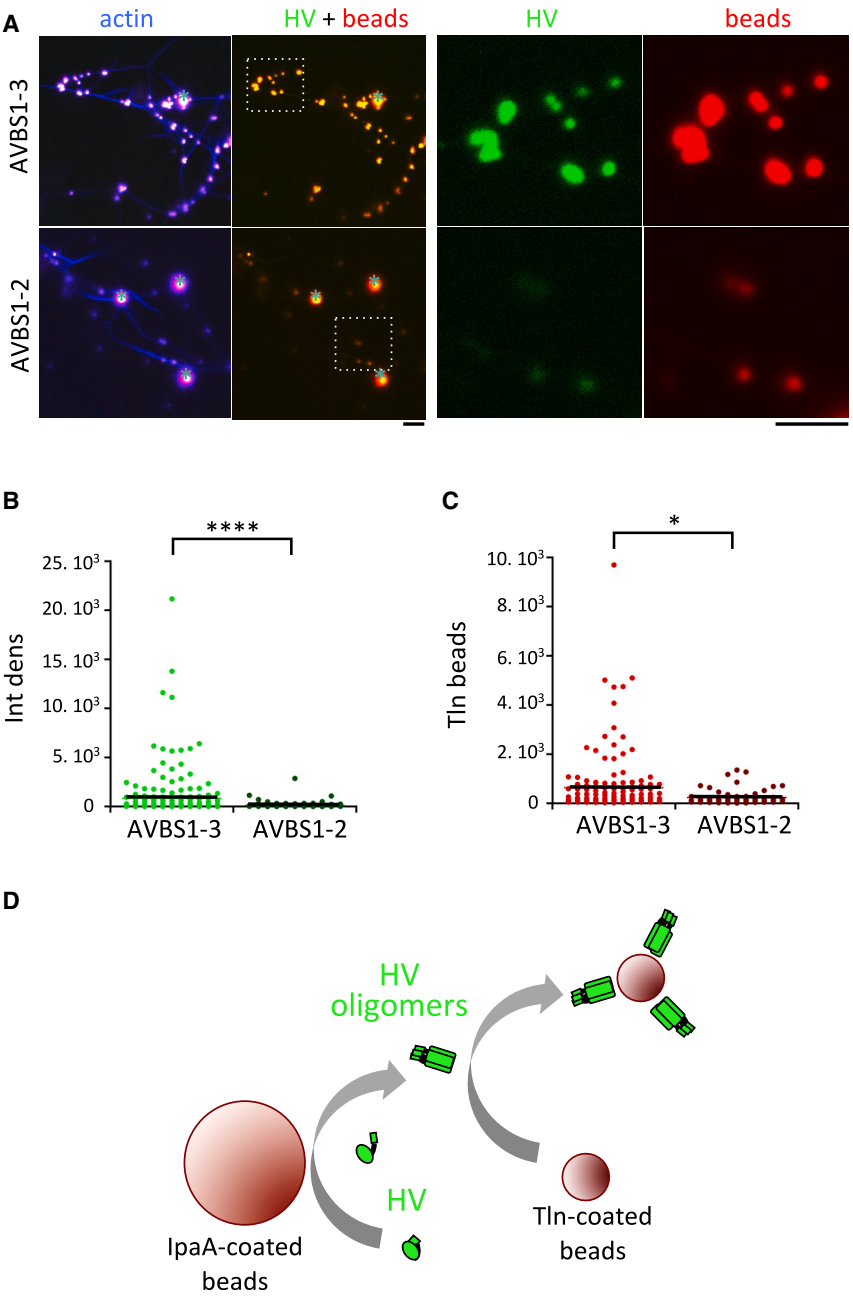

Figure 5. Vinculin oligomers are clustered by talin VBSs

Fluorescent actin was allowed to polymerize in the presence of vinculin, 1 μm diameter red fluorescent beads coated with the indicated sample and 100 nm diameter red fluorescent beads coated with talin H1-H4.

(A) Representative micrographs. Blue: actin. Green: vinculin. Red: 1 μm and 100 nm red fluorescent coated beads. The cyan stars indicate GST-AVBS1–2-/GST-AVBS1–3-coated 1 μm beads. Right panels are higher magnification of the insets shown in the left panels. Scale bar: 1 μm.

(B) Normalized integrated density of vinculin clusters. HV+AVBS1–3: 204 clusters, N = 2; HV+AVBS1–2: 142 clusters, N = 2.

(C) Normalized integrated density talin H1-H4 beads. HV+AVBS1–3, 148 clusters, N = 2; HV+AVBS1–2: 64 clusters, N = 2. Mann and Whitney. *p = 0.023; ****p = 0.00018.

(D) Model for vinculin oligomers clustering by talin VBSs. Bead-immobilized AVBS1–3 catalyze the formation of vinculin oligomers, which diffuse away from activation site. Vinculin oligomers binding to talin (Tln)-coated beads results in higher-order cluster formation.

Talin VBSs promote higher-order clustering of IpaA-induced vinculin oligomers

During canonical activation, vinculin simultaneously binds to talin and actin filaments through its N-terminal and C-terminal domains. We then used fluorescent vinculin clustering assays to ask whether, in addition to actin bundling, AVBS1–3-mediated vinculin oligomers could interact with talin. In the design of these experiments, we aimed to mimic the multiplicity of VBSs present per talin molecule expected to play an additional scaffolding role in vinculin cluster formation at FAs. For this purpose, we coated 100 nm beads with the vinculin binding H1-H4 helices from the R1 talin bundle at a calculated density of one H1H4 molecule/86 nm^2 and co-incubated these beads along with AVBS1–3-coated beads and vinculin in actin polymerization assays. As shown in Figure 5A, talin (Tln) beads co-localized with vinculin clusters induced by AVBS1–3-coated beads, consistent with binding of vinculin oligomers to talin. As expected, very few clusters were observed for AVBS1–2-coated beads (Figure 5A). In addition, the integrated density of vinculin clusters showed a striking difference between AVBS1–2 and AVBS1–3, with AVBS1–3-induced clusters being, on average, 9 times brighter than AVBS1–2-induced clusters (Figures 5A, left panels, and 5B). These marked differences suggested additional clustering levels mediated by multivalent talin beads. To confirm this, we quantified the density of talin beads per vinculin clusters based on their integrated fluorescence intensity. As shown in Figure 5C, talin beads showed a recruitment that was 2.3-fold higher at vinculin clusters induced by AVBS1–3 relative to AVBS1–2, suggestive of higher-order clustering.

Together, the results indicate that as opposed to canonical activation, vinculin supra-activation leads to the formation of homo-oligomers mediating actin bundling and binding to talin, a property promoting another level of clustering by multivalent VBSs. Following diffusion, vinculin oligomers show persistent F-actin binding and bundling activity at a distance from the activation site.

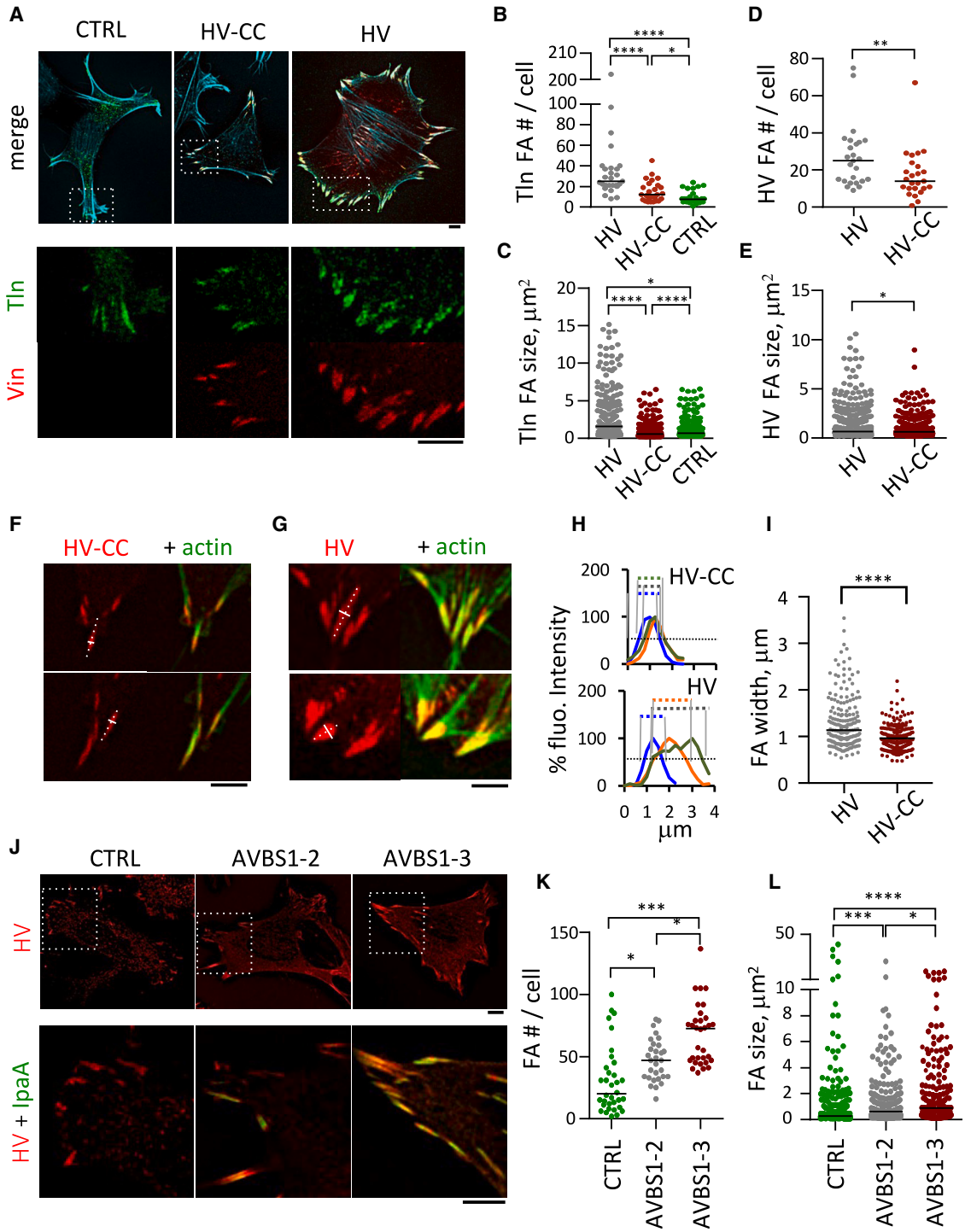

Figure 6. Vinculin supra-activation promotes the merging of adhesions clusters

Cells were transfected, fixed, and processed for fluorescence microscopy analysis of FAs.

(A, F, G, and J) Representative fluorescence micrographs. Red: vinculin-mCherry; green: GFP-talin (A) or F-actin (F and G); cyan: F-actin (A). Scale bar: 5 µm.

(A–I) MEF vinculin-null cells; transfection with GFP-talin (CTRL); talin co-transfection with full-length HV-mCherry (HV) or HV Q68C A396C-mCherry (CC-HV).

(J–L) C2.7 cells; transfection with vinculin (CTRL); vinculin co-transfection with GFP-AVBS1–2 or GFP-AVBS1–3.

(B–E, K, and L) The FA number per cell and size were determined using a semi-automatic detection program (STAR Methods). Bar: median size. FAs analyzed for (B and C) GFP-talin and (D, E, H, I, K, and L) HV or CC-HV.

(legend continued on next page)

Vinculin supra-activation promotes actin bundling and adhesion expansion

We next tested the effects of vinculin supra-activation on FA formation by introducing the cysteine clamp in full-length vinculin fused to mCherry (CC-HV) and analyzed its effects following transfection in mouse embryonic fibroblast (MEF) vinculin-null cells. As shown in Figure 6A, vinculin led to the formation of larger and more numerous talin-containing FAs than mock-transfected vinculin-null cells, consistent with residual vinculin activation (Figures 6A and 6B). In contrast, CC-HV-expressing cells formed significantly fewer and smaller FAs than cells transfected with vinculin (Figures 6A–6E). A more detailed analysis indicated that the average width of adhesions formed by CC-HV was remarkably conserved with an average of 0.96 ± 0.27 (SD) μm (Figures 6F, 6H, and 6I). This was in sharp contrast to FAs formed by WT vinculin showing a larger dispersion in average width (1.31 ± 0.57 [SD] μm) and reaching up to several μm (Figures 6G–6I). In addition, stress fibers and thick actin bundles connecting FAs were observed for HV-, but not CC-HV-, expressing cells (Figures 6A, 6F, and 6G). These results suggest that vinculin supra-activation impaired in CC-HV is involved in the growth of adhesion structures and actin bundling during FA maturation.

To clarify the role of IpaA-mediated vinculin supra-activation in FA dynamics, we analyzed the effects of AVBS1–2 and AVBS1–3 expression in C2.7 cells, a vinculin-expressing myoblastic cell line, which form prominent FAs well suited for dynamic TIRF (total internal reflection fluorescence) microscopy analysis. As shown in Figures 6J–6L, S8A, and S8B, cells transfected with GFP-AVBS1–2 formed more numerous and larger peripheral FAs as well as actin-rich ruffles compared with control cells. GFP-AVBS1–3-transfected cells formed even larger and more numerous FAs but with significantly less actin ruffles than GFP-AVBS1–2-transfected cells (Figures 6J–6L, S8A, and S8B). Strikingly, GFP-AVBS1–3-induced FAs were extremely stable, with a median duration of at least 84 min, while GFP-AVBS1–2-transfected and control cells showed FAs with a comparable median duration of less than 25 min (Figures S8C and S8D; Video S1). This increased FA stability in GFP-AVBS1–3 transfectants was predominantly due to decreased rates of FA disassembly with a 2-fold decrease in median instant rates relative to control cells (Figures S8E and S8F; Video S1). These results indicate that AVBS1–3-induced vinculin supra-activation promotes the expansion and increased stability of FAs.

IpaA-induced FAs form independent of mechanotransduction

The stability of IpaA-induced FAs suggests that their formation may be less dependent on mechanotransduction. To test this, we analyzed the effects of the acto-myosin relaxing Rho-kinase inhibitor Y27632. Strikingly, vinculin-labeled FAs induced by GFP-AVBS1–3 resisted the action of Y27632, with five and four times slower median rates of FA disassembly relative to control cells and GFP-AVBS1–2 transfectants, respectively (Figures 7A–7C; Video S2). Large FAs were even observed to form in GFP-AVBS1–3 transfectants following addition of the inhibitor (Figures 7A–7C), a process that was not observed for other samples, including cells transfected with GFP fused to the vinculin D1 domain (vD1) reported to delay talin refolding following stretching[22–24] (Figures 7A–7C; Video S2). GFP-AVBS1–3 also delayed the Y27632-induced removal of the late adhesion marker VASP (Figure S9; Video S3).

These findings are consistent with our *in vitro* results showing the catalysis by IpaA of vinculin oligomers with persistent activity. The resistance of VASP to the action of Y27632 in IpaA-induced FAs suggests that vinculin oligomers contribute to the scaffolding of this late FA marker.

DISCUSSION

Shigella invades host cells through a triggering mode implicating a discrete number of contacts between the type III secretion system (T3SS) and host cells.[2] How IpaA promotes bacterial attachment to the cell surface by reinforcing cytoskeletal tethering to limited bacterial contact sites has been an open question. Here, we show that IpaA induces the supra-activation of vinculin associated with unveiling of binding sites on the D2 subdomain and major conformational changes of the vinculin head. Vinculin supra-activation leads to the formation of vinculin homo-oligomers that bundle actin filaments and bind to talin. Strikingly, IpaA-induced vinculin oligomers diffuse away from activation sites, a property associated with the expansion of adhesion structures at bacterial contact sites during *Shigella* invasion. Our studies also suggest that vinculin supra-activation is also involved in the maturation of cell adhesions, independent of bacterial invasion: (1) a cysteine clamp inhibiting vinculin supra-activation, but not canonical activation, prevents the formation of mature adhesions, and (2) IpaA VBS1–3, which mediate vinculin supra-activation, accelerate the speed of cell adhesion but at a steady state, and the strength of cell adhesion does not differ from that of control cells. These results suggest that IpaA VBS1–3 mediate vinculin supra-activation through the unique organization and joint action of its three VBSs but that canonical activation also leads to supra-activation when combined with mechanotransduction. Consistent with this, we also found that during *Shigella* invasion, vinculin supra-activation triggered by IpaA VBS1–3 is required for full adhesion formation at bacterial contact sites, while canonical activation mediated by a single IpaA VBS is sufficient for FA formation at basal membranes distal from bacteria.

(B–E) CTRL: n = 28, N = 3; HV: n = 25, N = 3; CC-HV: n = 25, N = 3.
(H) Three representative plot profiles (blue, orange, and green) from separate linescans, illustrated by the ones shown in solid white lines orthogonal to the main FA axis (dashed white lines) in (F) and (G).
(I) FA width determined as the full width half-maximum by linear interpolation from plot profiles in (H); HV: 181 FAs, 6 cells, N = 2. CC-HV: 101 FAs, 14 cells, N = 3. Mann-Whitney test with Bonferroni multiple comparison correction. *p < 0.05; **p < 0.01; ***p < 0.005; ****p < 0.001.
(J–L) n > 30 cells, N = 3. Dunn's multiple comparisons test. *p < 0.05; ***p < 0.005.

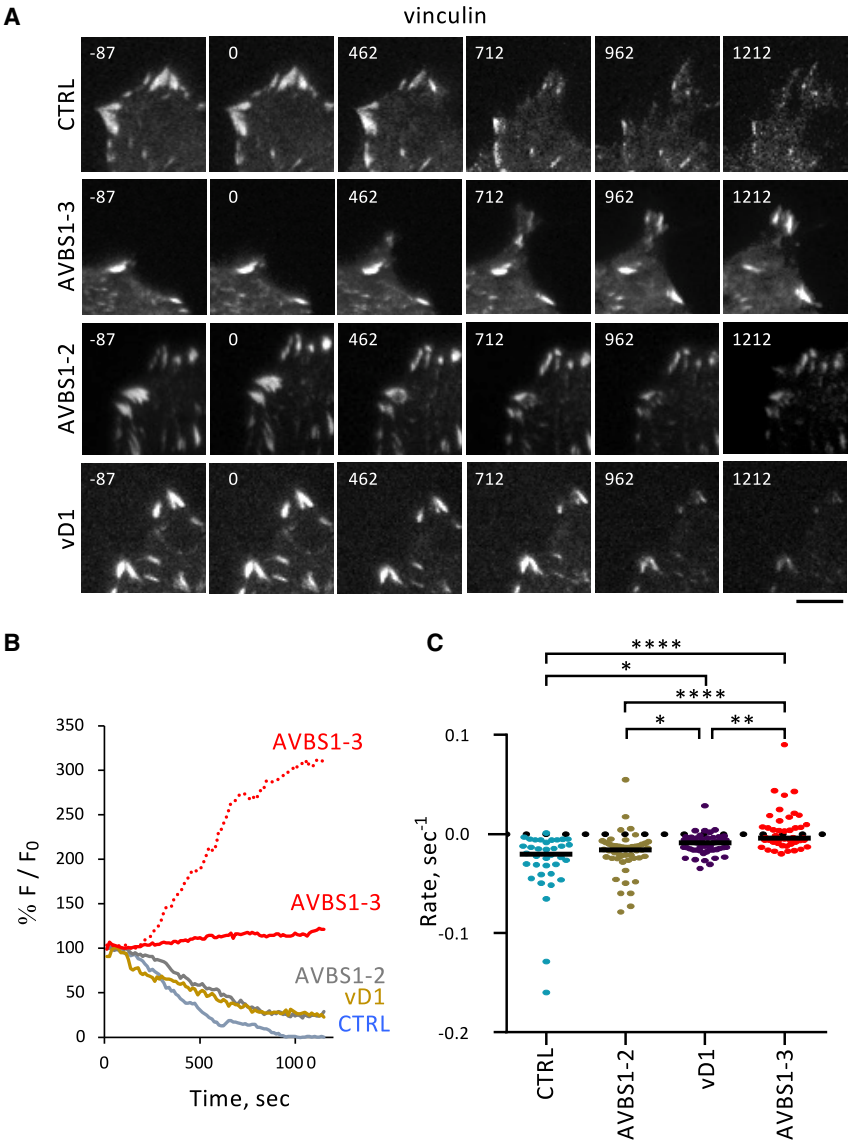

Figure 7. IpaA-mediated vinculin supra-activation stimulates cell adhesion independent of mechanotransduction

TIRF microscopy of C2.7 cells transfected with mCherry-vinculin alone (CTRL) or co-transfected with GFP-AVBS1–2 (AVBS1–2), GFP-vD1 (vD1), or GFP-AVBS1–3 (AVBS1–3). Adhesion kinetic parameters were determined from time-lapse acquisitions following cell treatment with 100 μM Y-27632.

(A) Representative time series acquisitions. Numbers indicated the elapsed time in seconds, with the inhibitor added at t = 0. Scale bar: 5 μm.

(B) % F/F_0: average fluorescence intensity of adhesions expressed as a percentage of initial fluorescence. Each solid line is a representative trace corresponding to a single adhesion for the indicated sample in the corresponding color. The dashed redline illustrates FA assembly in GFP-AVBS1–3-transfected cells, which was seldom observed with the other samples.

(C) Initial rates of adhesion assembly/disassembly inferred from linear fits. Number of adhesions analyzed: N = 5. CTRL: 84; vD1: 75; AVBS1–2: 140; AVBS1–3: 97. Dunn's multiple comparisons test. *p < 0.05; ****p < 0.001.

Interestingly, molecular dynamics simulations suggest that stretching of the vinculin during mechanotransduction also results in the exposure of the vinculin head D2 subdomain.[25] It is therefore tempting to speculate that mechanotransduction also leads to the vinculin homo-oligomerization that we observed for IpaA through intermolecular interactions between the D1-D2 domains. Whether vinculin stretching alone, or an additional interaction between a VBS and D2 in a manner similar to IpaA VBS3, is required during mechanotransduction is not known. Of interest, IpaA VBS3 shares homology with the talin VBS corresponding to helix 46.[5] This suggests that talin H46 helix could play such a role during vinculin supra-activation.

There are important differences, however, that one can expect from vinculin supra-activation depending on IpaA or mechanotransduction. These differences could account for the extreme stability of FAs in IpaA VBS1–3 compared with IpaA VBS1–2 transfectants during cell treatment with actin relaxing drugs. Indeed, IpaA acts as a catalyst leading to the persistent production of vinculin oligomers independent of the stretching of vinculin by cytoskeletal forces. During vinculin canonical activation, however, oligomers will form as a function of the stretching force and disassemble when the force is released.

Vinculin oligomers are sufficiently biochemically stable to be observed in our SEC-MALS, native gel, or fluorescence microscopy analysis, suggesting the stabilization of conformers via interprotomer interactions. Because of this property, vinculin supra-activation may correspond to a switch defining a threshold during the formation of adhesion structures. Indeed, because of their relative stability and their ability to simultaneously bundle actin filaments, bind to talin, and diffuse away from activation sites, vinculin oligomers following supra-activation are expected to promote the expansion and strengthening of adhesion structures through diffusion and capture by talin VBSs. Consistently, our studies show that supra-activation-deficient cysteine-clamped vinculin only supports the formation of small adhesion structures (<1 μm width) with limited actin bundling, while supra-activation-proficient vinculin promotes the formation of large FAs and actin bundles. Our talin-bead scaffolding assays indicate that vinculin cluster formation is further driven by the multiplicity of talin VBSs (Figure S10, gray arrows). Because of the multiplicity of VBSs on talin molecules, co-clustering between vinculin oligomers and talin is likely to

play a role in adhesion expansion (Figure S10). Vinculin has been shown to immobilize and bundle actin filaments from Arp2/3 branched networks.[20] In this case, however, bundling was shown to occur at activation sites and was proposed to occur through talin-vinculin scaffolds.[20] This activity is in contrast to diffusible bundling activity associated with vinculin oligomers that we describe here, which may promote clustering at a distance from activation sites. Clustering of adhesions at different scales is believed to play a major role in adhesive processes through the regulation of functional units.[26] At the molecular levels, integrin clustering in adhesions is not fully understood; it may be induced by ligand binding and integrin homo-oligomerization via integrin transmembrane domains.[27] Nanoclusters consisting of hundreds of integrin molecules were proposed to correspond to elementary units that merge to form nascent adhesions.[28] Vinculin oligomers following supra-activation could provide an additional basis for the expansion of adhesions through the bundling of actin filaments and scaffolding of cytoskeletal linkers in response to increasing acto-myosin pulling force (Figure S10). As opposed to physiological substrates, single bacteria cannot sustain the range of counterforces associated with the strengthening of adhesion structures during mechanotransduction and integrin-mediated adhesion to the substrate. Actin bundling and scaffolding triggered by IpaA-induced vinculin oligomers may provide *Shigella* with the means to strengthen its adhesion during bacterial invasion independent of mechanotransduction (Figure S10). Importantly, the view of IpaA catalyzing the formation of vinculin-activated vinculin oligomers may explain its potency and how a limited number of this injected type III effector can have major impact on the global cell adhesion properties, distal from bacterial invasion sites (Figure S10). Understanding how vinculin supra-activation and oligomer formation regulate the composition and properties of adhesions at *Shigella* invasion sites will likely have important implications for cell adhesion and will be the focus of future investigation.

Limitations of the study

We describe a mode of vinculin supra-activation induced by the *Shigella* type III effector IpaA. Whether vinculin supra-activation also occurs during cell adhesion during the maturation of adhesion structures will require further investigation.

STAR★METHODS

Detailed methods are provided in the online version of this paper and include the following:

SUPPLEMENTAL INFORMATION

Supplemental information can be found online at https://doi.org/10.1016/j.celrep.2023.112405.

ACKNOWLEDGMENTS

The authors thank Gauthier Mercante for technical help, Philippe Mailly for help with image analysis, and René-Marc Mège for insightful discussions and reading of the manuscript. This work was supported by grants from INSERM, CNRS and Collège de France to the CIRB, as well as by a grant from the PSL Idex project "Shigaforce." D.-I.A.S. and B.C.-C. are recipients of a PhD fellowship from a CONACYT scholarship. C.V.-G. and D.-I.A.S. also received support from the Memolife Labex. H.K. and L.M. were supported by Swiss National Science Foundation (grant no. SNF P2ZHP3_191289) and the Knut and Alice Wallenberg Foundation (grant no. KAW 2016.0023), respectively. This work benefited from the facilities and expertise of the Macromolecular Interaction Platforms of I2BC.

AUTHOR CONTRIBUTIONS

C.V.-G. and D.-I.A.S. conceived and performed most of the experimental works and data analysis and wrote the manuscript. B.C.-C., S.E., and B.M. analyzed TIRF experiments. C.V. and C.B.-N. performed the SEC-MALS analysis. B.C.-C. and Y.Z. performed native gel analysis of vinculin complexes. C.M. and J.C.-R. designed and performed the LC-MS analysis. D.B.L. analyzed the cross-linked MS data. H.K. and L.M. generated structural models. C.L.C. provided help for the actin co-sedimentation assays. G.T.V.N. designed the project and wrote the manuscript.

DECLARATION OF INTERESTS

The IpaA constructs in this study are associated with the patent N°PVT/EP2016/073287.2016 with no restriction for academic research but with restriction for commercial use.

Received: January 3, 2022
Revised: February 22, 2023
Accepted: April 3, 2023
Published: April 17, 2023

REFERENCES

1. Ogawa, M., Handa, Y., Ashida, H., Suzuki, M., and Sasakawa, C. (2008). The versatility of Shigella effectors. Nat. Rev. Microbiol. *6*, 11–16.
2. Valencia-Gallardo, C.M., Carayol, N., and Tran Van Nhieu, G. (2015). Cytoskeletal mechanics during Shigella invasion and dissemination in epithelial cells. Cell Microbiol. *17*, 174–182.
3. Mattock, E., and Blocker, A.J. (2017). How do the virulence factors of Shigella work together to cause disease? Front. Cell. Infect. Microbiol. *7*, 64.
4. Romero, S., Grompone, G., Carayol, N., Mounier, J., Guadagnini, S., Prevost, M.C., Sansonetti, P.J., and Tran Van Nhieu, G. (2011). ATP-mediated Erk1/2 activation stimulates bacterial capture by filopodia, which precedes Shigella invasion of epithelial cells. Cell Host Microbe *9*, 508–519.
5. Valencia-Gallardo, C., Bou-Nader, C., Aguilar-Salvador, D.I., Carayol, N., Quenech'Du, N., Pecqueur, L., Park, H., Fontecave, M., Izard, T., and Tran Van Nhieu, G. (2019). Shigella IpaA binding to talin stimulates filopodial capture and cell adhesion. Cell Rep. *26*, 921–932.e6.
6. Humphries, J.D., Wang, P., Streuli, C., Geiger, B., Humphries, M.J., and Ballestrem, C. (2007). Vinculin controls focal adhesion formation by direct interactions with talin and actin. J. Cell Biol. *179*, 1043–1057.
7. Ciobanasu, C., Faivre, B., and Le Clainche, C. (2014). Actomyosin-dependent formation of the mechanosensitive talin-vinculin complex reinforces actin anchoring. Nat. Commun. *5*, 3095. https://doi.org/10.1038/ncomms4095.
8. Atherton, P., Stutchbury, B., Wang, D.Y., Jethwa, D., Tsang, R., Meiler-Rodriguez, E., Wang, P., Bate, N., Zent, R., Barsukov, I.L., et al. (2015). Vinculin controls talin engagement with the actomyosin machinery. Nat. Commun. *6*, 10038. https://doi.org/10.1038/ncomms10038.
9. Izard, T., Tran Van Nhieu, G., and Bois, P.R.J. (2006). Shigella applies molecular mimicry to subvert vinculin and invade host cells. J. Cell Biol. *175*, 465–475.
10. Tran Van Nhieu, G., and Izard, T. (2007). Vinculin binding in its closed conformation by a helix addition mechanism. EMBO J. *26*, 4588–4596.
11. Bakolitsa, C., Cohen, D.M., Bankston, L.A., Bobkov, A.A., Cadwell, G.W., Jennings, L., Critchley, D.R., Craig, S.W., and Liddington, R.C. (2004). Structural basis for vinculin activation at sites of cell adhesion. Nature *430*, 583–586.
12. Izard, T., Evans, G., Borgon, R.A., Rush, C.L., Bricogne, G., and Bois, P.R.J. (2004). Vinculin activation by talin through helical bundle conversion. Nature *427*, 171–175.
13. Park, H., Valencia-Gallardo, C., Sharff, A., Tran Van Nhieu, G., and Izard, T. (2011). Novel vinculin binding site of the IpaA invasin of Shigella. J. Biol. Chem. *286*, 23214–23221.
14. Johnson, R.P., and Craig, S.W. (2000). Actin activates a cryptic dimerization potential of the vinculin tail domain. J. Biol. Chem. *275*, 95–105.
15. Janssen, M.E.W., Kim, E., Liu, H., Fujimoto, L.M., Bobkov, A., Volkmann, N., and Hanein, D. (2006). Three-dimensional structure of vinculin bound to actin filaments. Mol. Cell *21*, 271–281.
16. Chinthalapudi, K., Rangarajan, E.S., Patil, D.N., George, E.M., Brown, D.T., and Izard, T. (2014). Lipid binding promotes oligomerization and focal adhesion activity of vinculin. J. Cell Biol. *207*, 643–656.
17. Shen, K., Tolbert, C.E., Guilluy, C., Swaminathan, V.S., Berginski, M.E., Burridge, K., Superfine, R., and Campbell, S.L. (2011). The vinculin C-terminal hairpin mediates F-actin bundle formation, focal adhesion, and cell mechanical properties. J. Biol. Chem. *286*, 45103–45115.
18. Molony, L., and Burridge, K. (1985). Molecular shape and self-association of vinculin and metavinculin. J. Cell. Biochem. *29*, 31–36.
19. Thompson, P.M., Tolbert, C.E., and Campbell, S.L. (2013). Vinculin and metavinculin: oligomerization and interactions with F-actin. FEBS Lett. *587*, 1220–1229.
20. Boujemaa-Paterski, R., Martins, B., Eibauer, M., Beales, C.T., Geiger, B., and Medalia, O. (2020). Talin-activated vinculin interacts with branched actin networks to initiate bundles. Elife *9*, e53990.
21. Hauri, S., Khakzad, H., Happonen, L., Teleman, J., Malmström, J., and Malmström, L. (2019). Rapid determination of quaternary protein structures in complex biological samples. Nat. Commun. *10*, 192.
22. del Rio, A., Perez-Jimenez, R., Liu, R., Roca-Cusachs, P., Fernandez, J.M., and Sheetz, M.P. (2009). Stretching single talin rod molecules activates vinculin binding. Science *323*, 638–641.
23. Margadant, F., Chew, L.L., Hu, X., Yu, H., Bate, N., Zhang, X., and Sheetz, M. (2011). Mechanotransduction in vivo by repeated talin stretch-relaxation events depends upon vinculin. PLoS Biol. *9*, e1001223.
24. Carisey, A., Tsang, R., Greiner, A.M., Nijenhuis, N., Heath, N., Nazgiewicz, A., Kemkemer, R., Derby, B., Spatz, J., and Ballestrem, C. (2013). Vinculin regulates the recruitment and release of core focal adhesion proteins in a force-dependent manner. Curr. Biol. *23*, 271–281.
25. Kluger, C., Braun, L., Sedlak, S.M., Pippig, D.A., Bauer, M.S., Miller, K., Milles, L.F., Gaub, H.E., and Vogel, V. (2020). Different vinculin binding sites use the same mechanism to regulate directional force transduction. Biophys. J. *118*, 1344–1356.
26. Mège, R.M., and Ishiyama, N. (2017). Integration of cadherin adhesion and cytoskeleton at adherens junctions. Cold Spring Harb. Perspect. Biol. *9*, a028738.
27. Karimi, F., O'Connor, A.J., Qiao, G.G., and Heath, D.E. (2018). Integrin clustering matters: a review of biomaterials functionalized with multivalent integrin-binding ligands to improve cell adhesion, migration, differentiation, angiogenesis, and biomedical device integration. Adv. Healthc. Mater. *7*, e1701324.
28. Changede, R., and Sheetz, M. (2017). Integrin and cadherin clusters: a robust way to organize adhesions for cell mechanics. Bioessays *39*, 1–12.
29. Mitrossilis, D., Fouchard, J., Guiroy, A., Desprat, N., Rodriguez, N., Fabry, B., and Asnacios, A. (2009). Single-cell response to stiffness exhibits muscle-like behavior. Proc. Natl. Acad. Sci. USA *106*, 18243–18248.
30. Ramarao, N., Le Clainche, C., Izard, T., Bourdet-Sicard, R., Ageron, E., Sansonetti, P.J., Carlier, M.F., and Tran Van Nhieu, G. (2007). Capping of actin filaments by vinculin activated by the Shigella IpaA carboxyl-terminal domain. FEBS Lett. *581*, 853–857.
31. de Chaumont, F., Dallongeville, S., Chenouard, N., Hervé, N., Pop, S., Provoost, T., Meas-Yedid, V., Pankajakshan, P., Lecomte, T., Le Montagner, Y., et al. (2012). Icy: an open bioimage informatics platform for extended reproducible research. Nat. Methods *9*, 690–696.
32. Song, Y., DiMaio, F., Wang, R.Y.R., Kim, D., Miles, C., Brunette, T., Thompson, J., and Baker, D. (2013). High-resolution comparative modeling with RosettaCM. Structure *21*, 1735–1742.
33. Gray, J.J. (2006). High-resolution protein-protein docking. Curr. Opin. Struct. Biol. *16*, 183–193.
34. Eubel, H., and Millar, A.H. (2009). Systematic monitoring of protein complex composition and abundance by blue-native PAGE. Cold Spring Harb. Protoc. *2009*. pdb prot5221.
35. Shevchenko, A., Tomas, H., Havlis, J., Olsen, J.V., and Mann, M. (2006). In-gel digestion for mass spectrometric characterization of proteins and proteomes. Nat. Protoc. *1*, 2856–2860.
36. Braakman, I., Lamriben, L., van Zadelhoff, G., and Hebert, D.N. (2017). Analysis of disulfide bond formation. Curr. Protoc. Protein Sci. *90*, 14.1.1–14.1.22. https://doi.org/10.1002/cpps.43.
37. Pant, B.D., Oh, S., and Mysore, K.S. (2021). Protocol for determining protein cysteine thiol redox status using western blot analysis. STAR Protoc. *2*, 100566.

38. Ciobanasu, C., Faivre, B., and Le Clainche, C. (2015). Reconstituting actomyosin-dependent mechanosensitive protein complexes in vitro. Nat. Protoc. *10*, 75–89.

39. Papagrigoriou, E., Gingras, A.R., Barsukov, I.L., Bate, N., Fillingham, I.J., Patel, B., Frank, R., Ziegler, W.H., Roberts, G.C.K., Critchley, D.R., and Emsley, J. (2004). Activation of a vinculin-binding site in the talin rod involves rearrangement of a five-helix bundle. EMBO J. *23*, 2942–2951.

40. Lima, D.B., de Lima, T.B., Balbuena, T.S., Neves-Ferreira, A.G.C., Barbosa, V.C., Gozzo, F.C., and Carvalho, P.C. (2015). SIM-XL: a powerful and user-friendly tool for peptide cross-linking analysis. J. Proteomics *129*, 51–55.

STAR★METHODS

KEY RESOURCES TABLE

REAGENT or RESOURCE	SOURCE	IDENTIFIER
Antibodies		
Vin11.5	Sigma-Aldrich	Cat# V4505; RRID: AB_477617
Polyclonal anti-Shigella serotype V lipopolysaccharide	Valencia-Gallardo et al.[5]	N/A
Bacterial and virus strains		
Shigella flexneri serotype V	Valencia-Gallardo et al.[5]	M90T
Shigella flexneri serotype V *ipaA* mutant	Valencia-Gallardo et al.[5]	M90T *ipaA*
Chemicals, peptides, and recombinant proteins		
N-hydroxysulfosuccinimide	MERCK	106627-54-7
1-ethyl-3-carbodiimide hydrochloride	Sigma-Aldrich	25952-53-8
N-ethylmaleimide	Sigma-Aldrich	128-53-0
dithiothreitol	Sigma-Aldrich	16096-97-2
PEG-Mal	Sigma-Aldrich	63187
BodipyTM FL NHS Ester	ThermoFisher	D2184
Y-27632	Sigma-Aldrich	129830-38-2
Experimental models: Cell lines		
HeLa cells	ATCC	ATCC CCL-2
C2.7 cells	Mitrossilis et al.[29]	N/A
MEF vinculin null cells	Humphries et al.[6]	N/A
Oligonucleotides		
5′ GCGCATATGCCAGTGTTTCATACG-3′	This study	vD1 For
5′-CGTCGACTCACCAGGCATCTTCATCGGC-3′	This study	vD1 Rev
5′-CGTCGACTCAGTGTACAGCTGCTTTG-3′	This study	vD2 Rev
5′-GAGACTGTTCAAACCACTGAGGATTGCATTTTGAAG-3′	This study	HV-Q68C mut
5′-ATCGATGCTGCTCAGAACTGGCTTTGCGATCCAAAT-3′	This study	HV-A396C mut
5′-ACCCGGGATCCCGCC-3′	This study	GFP-vD1 For
5′-ACCCGGGACCAGGCA-3′	This study	GFP-vD1 Rev
5′-TCAAAGGACATTACAAAATCC-3′	This study	GFP-AVBS1-2 For
5′-GCGATATCATGGCCAGCAAAGG-3′	This study	GFP-AVBS1-3 For
5′-GCGCGGCCGCTTAATCCTTATTGATATTC-3′	This study	GFP-AVBS Rev
5′-GGCGAATTCCCGGAGACACATATTTAACACG-3′	This study	GST-AVBS1-3 For
5′-GCCGTCGACTTAATCCTTATTGATATTCT-3′	This study	GST-AVBS1-3 Rev
5′-ACCCGGGATCCCGCC-3′	This study	GFP-vD1 For
5′-ACCCGGGACCAGGCA-3′	This study	GFP-vD1 Rev
Recombinant DNA		
pET15b-D1	This study	N/A
pET15b-D1D2	This study	N/A
pET15b-D1D2-CC	This study	N/A
pGFP-vD1	This study	N/A
pmCherry N1-HV-CC	This study	N/A
pGFP-AVBS1-2	This study	N/A
pGFP-AVBS1-3	This study	N/A
pGST-AVBS1-2	Ramarao et al.[30]	N/A
pGST-AVBS1-3	This study	N/A
pC1-HV8His	This study	N/A

(*Continued on next page*)

Continued

REAGENT or RESOURCE	SOURCE	IDENTIFIER
pC1HV-CC8His	This study	N/A
pmCherry-human vinculin	Addgene	55160
pmCherry-VASP	Addgene	55151
Software and algorithms		
Icy	De Chaumont et al. [31]	N/A
Rosetta modeling	Song et al.[32]	N/A
RosettaDock	Gray[33]	N/A
ASTRA 6.1.7.17	Wyatt Technology Europe	N/A

RESOURCE AVAILABILITY

Lead contact

Further information and requests for resources and reagents should be directed to the lead contact, Guy Tran Van Nhieu (guy.tranvannhieu@i2bc.paris-saclay.fr).

Materials availability

The IpaA derivative constructs in this study are associated with the patent N°PVT/EP2016/073287. 2016 with no restriction for academic research, but restriction for commercial use.

Data and code availability

All data reported in this paper will be shared by the lead contact upon request. Any additional information required to reanalyze the data reported in this paper is available from the lead contact upon request. This paper does not report original code.

EXPERIMENTAL MODEL AND SUBJECT DETAILS

Cell lines and bacterial strains

HeLa cells (ATCC CCL-2) were incubated in RPMI (Roswell Park Memorial Institute) medium containing 5% FCS (fetal calf serum, Gibco) in an incubator with 5% CO_2. C2.7 myoblasts,[29] MEF and MEF vinculin null cells (Humphries, Wang et al. 2007) were routinely grown in DMEM 1 g/L glucose containing 10% FCS in a 37°C incubator containing 10% CO_2. For transfection experiments, cells were seeded at 2.5 x 10^4 cells in 25 mm-diameter coverslips. Cells were transfected with 3 μg of pGFP-AVBS1-2 or pGFP-AVBS1-3 plasmids with 6 μL JetPEI transfection reagent (Polyplus) for 16 h following the manufacturer's recommendations. C2.7 mice myoblasts cells were fixed in PBS containing 3.7% paraformaldehyde for 20 min at 21°C and permeabilized with 0.1% Triton X-100 for 4 min at 21°C.

The wild type *Shigella flexneri*, isogenic mutants, and complemented *ipaA* mutant strains, as well as wild type *Shigella* expressing the AfaE adhesin were previously described.[9] Bacterial strains were cultured in trypticase soy broth (TCS) medium at 37°C. When specified, antibiotics were added at the following concentrations: carbenicillin 100 μg/mL, kanamycin 20 μg/mL.

Plasmids and constructs

Human vinculin constructs were generated by polymerase chain reaction using the forward primer 5′ GCGCATATGCCAGTGT TTCATACG-3′ and reverse primers 5′-CGTCGACTCACCAGGCATCTTCATCGGC-3′ for D1 (residues 1–258) or 5′-CGTCGACTCA GTGTACAGCTGCTTTG-3′ for D2 (residues 1–492) using a plasmid containing full-length octahistidine-tagged human vinculin (pET3a-vinculin 8His, residues 1–1,066), as template,[11] and cloned into the NdeI-SalI sites of pet15b (Novagen) to obtain pET15b-D1 and pET15b-D1D2, respectively. The Q68C and A396C cysteine substitution for the cysteine clamp were introduced into pet15b-D1D2 by site-directed mutagenesis using the 5′-GAGACTGTTCAAACCACTGAGGATTGCATTTTGAAG-3′ and 5′-ATCG ATGCTGCTCAGAACTGGCTTTGCGATCCAAAT-3′ primers, respectively. The pGFP-vD1 plasmid was generated by polymerase chain reaction using the forward primer 5′-ACCCGGGATCCCGCC-3′ and reverse primer 5′-ACCCGGGACCAGGCA-3′, and cloned into pEGFP. The pmCherry-human vinculin (HV) and pmCherry-VASP plasmids were from Addgene. Stealth siRNA anti-human vinculin was from Invitrogen (reference number 1299001). The cysteine clamp was introduced in pmCherry N1-vinculin by exchanging the NheI-PspXI fragment with the corresponding XbaI-PspXI fragment of pET15b-D1D2 -Q68C A396C. Introduction of the cysteine clamp in full length vinculin was performed by swapping the *SexAI-BsrgI* fragment from pET15b-D1D2-Q68C-A396C and pET3a-vinculin 8His.

The IpaA constructs GFP-AVBS1-2 and GFP-AVBS1-3 were generated by polymerase chain reaction (PCR) and cloning into pcDNA3.1 NT-GFP Topo TA (Invitrogen) using the 5′-TCAAAGGACATTACAAAATCC-3′ and 5′-GCGATATCATGGCCAGCAAAGG-3′ forward primers, respectively, and the 5′-GCGCGGCCGCTTAATCCTTATTGATATTC-3′ reverse primer. The GST-AVBS1-3 construct was generated by PCR using 5′-GGCGAATTCCCGGAGACACATATTTAACACG-3′ forward and 5′-GCCGTCGACTTA ATCCTTATTGATATTCT-3′ reverse primers and cloning into the *EcoRI-SalI* ofpGEX-4T-2 (GE Lifesciences). pGST-AVBS1-2 was previously described.[30] The pGFP-vD1 plasmid was generated by polymerase chain reaction using the forward primer 5′-ACC CGGGATCCCGCC-3′ and reverse primer 5′-ACCCGGGACCAGGCA-3′, and cloned into pEGFP. The pmCherry-human vinculin (HV) and pmCherry-VASP plasmids were from Addgene. Stealth siRNA anti-human vinculin was from Invitrogen (reference number 1299001). All constructs were verified by DNA sequencing. Plasmids pC1-HV8His and pC1HV-CC8His were generated by replacing the 1.1 kb EcoRV-NotI fragment of pmCherryN1-HV and pmCherryN1-HV-CC, respectively, by the 764 bp EcoRV-NotI fragment from pET3a-vinculin 8His.

METHOD DETAILS

Cell challenge with *Shigella* strains

HeLa cells seeded at 4 x 10^5 cells in coverslip-containing 34 mm-diameter wells the day before the experiment. After 16 h, cells were challenged with *Shigella* strains coated with poly-L-lysine, as follows. Bacteria grown to an $OD_{600\ nm}$ of 0.6–0.8 were washed three-times by successive centrifugation at 13 kg for 30 s and resuspension in EM buffer (120 mM NaCl, 7 mM KCl, 1.8 mM $CaCl_2$, 0.8 mM $MgCl_2$, 5 mM glucose, and 25 mM HEPES, pH = 7.3). Samples were resuspended in EM buffer containing 50 μg/mL poly-L-lysine and incubated for 15 min at 21°C, washed three times in EM buffer and resuspended in the same buffer at a final OD of $OD_{600\ nm}$ = 0.2. Cell samples were washed three times in EM buffer and challenged with 1 mL of the bacterial suspension and incubated at 37°C. Samples were fixed with PBS containing 3.7% PFA after 30 min incubation. Samples were processed for immunofluorescence microscopy.

Immunofluorescence staining

Cells were processed for immunofluorescence staining using the Vin11.5 anti-vinculin monoclonal antibody (ref. V4505, Sigma-Aldrich) and anti-mouse IgG antibody coupled to Alexa 546 (Jackson Research) and Phalloidin-Alexa 633 (Invitrogen), as described previously.[10] Bacteria were labeled using anti-LPS rabbit polyclonal antibody followed by anti-rabbit IgG antibody coupled to Alexa 525 as described.[9] Samples were analyzed using an Eclipse Ti inverted microscope (Nikon) equipped with a 60× objective, a CSU-×1 spinning disk confocal head (Yokogawa), and a Coolsnap HQ2 camera (Roper Scientific Instruments), controlled by the Metamorph 7.7 software. Analysis of fluorescent actin filaments was performed using a Leica confocal SP8 using a 63× objective.

Protein purification

BL21 (DE3) chemically competent *E. coli* (Life Technologies) was transformed with the expression constructs. D1 and D1D2 were purified essentially as described.[13,34] For the IpaA derivatives, bacteria grown until OD_{600nm} = 1.0 were induced with 0.5 mM IPTG and incubated for another 3 h. Bacteria were pelleted and washed in binding buffer 25 mM Tris PH 7.4, 100 mM NaCl and 1 mM beta-mercaptoethanol, containing Complete™ protease inhibitor. Bacterial pellets were resuspended in 1/50th of the original culture volume and lyzed using a cell disruptor (One shot model, Constant System Inc.). Proteins were purified by affinity chromatography using a GSTrap HP affinity column (GE Healthcare) and size exclusion chromatography (HiLoad S200, GE Healthcare). Samples were stored aliquoted at −80°C at concentrations ranging from 1 to 10 mg/mL.

Protein complex formation analysis

Proteins were incubated at a concentration of 30 μM in binding buffer for 60 min at 4°C. Samples were analyzed by SEC-MALS using an HPLC (Shimadzu), a 24 mL Superdex 200 Increase 10/300 GL filtration column (GE Healthcare) and a MiniDAWN TREOS equipped with a refractometer Optilab T-rEX (Wyatt Technology) connected in series, to separate constructs according to their Stokes radius and determine the molar mass of macromolecules in solution. Data were analyzed using the ASTRA 6.1.7.17 software (Wyatt Technology Europe). Protein complex formation was visualized by PAGE under non-denaturing conditions using à 7.5% polycrylamide gel, followed by Coomassie blue staining.

Solid-phase binding assay

96–well Maxisorp (Nunc) ELISA plates were coated with 30 nM of full-length vinculin, vinculin constructs or IpaA proteins at the indicated concentrations in binding buffer (25 mM Tris PH 7.4, 100 mM NaCl and 1 mM β-mercaptoethanol). Samples were blocked with PBS-BSA 2%, washed and incubated with IpaA or vinculin proteins in binding buffer containing 0.2% BSA at room temperature for 1 h. After incubation, the plates were washed and incubated with an anti-IpaA (dilution 1/2000^e) polyclonal primary antibody[3] or anti-vinculin (dilution 1/2000^e) Vin11.5 monoclonal antibody (Sigma-Aldrich) in binding buffer containing 0.2% BSA for 1 h at room temperature. Plates were washed and incubated with an HRP-coupled secondary anti-rabbit or anti-mouse IgG antibody (1/32000^e) (Jackson ImmunoResearch) for 1 h. The reaction was revealed by adding 100 μL of tetramethylbenzidine (Sigma-Aldrich) for 15 min, stopped by adding 50 μL of 0.66N H_2SO_4 and the absorbance was read at 450 nm (Dynatech MR400).

BN-PAGE (blue native – Polyacrylamide gel electrophoresis) protein native gel analysis and complex cross-linking

25 μM of vinculin constructs were incubated with different molar ratios of IpaA proteins in a 1X BN-PAGE buffer (250 mM ε-aminicaprionic acid and 25 mM Bis-Tris PH 7,0) at 4°C for 1 h. The protein mixtures were separated in a one-dimension native BN-PAGE electrophoresis as described[34] (Figure S3). For vinculin-IpaA protein ratio assay, vinculin-IpaA bands containing the complexes separated by BN-PAGE were cut, sliced and boiled in 2 x Laemmli SDS buffer followed by SDS-PAGE. The second dimension SDS-PAGE gels were stained (colloidal Coomassie staining) and the density of the bands was determined using ImageJ. The normalized vinculin:IpaA ratio of the complexes was compared using a non-parametric Kruskal-Wallis rank-sum test (R statistical software).

For crosslinking vinculin-IpaA complex, bands containing the complexes were cut, sliced and electroeluted in native conditions (15 mM Bis-Tris pH 7.0 and 50 mM Tricine) inside a closed dialysis membrane (SpectraPor). The soluble complexes were recovered and their buffer exchanged twice into an amine-free cross-link buffer in 25 mM HEPES pH 7.0 containing 100 mM NaCl using 10MWCO ZEBA desalting columns (Thermo Scientific). The fractions containing the complexes were incubated for 1 h at 4°C with 10 mM N-hydroxysulfosuccinimide and 5 mM EDC (Sigma-Aldrich) following the manufacturer's recommendations. The cross-linking reaction was stopped by adding 50 mM Tris pH 7.4 and incubating for 20 min. Samples were denaturated in 2x SDS Laemmli buffer for 5 min at 95°C and complexes were eluted from gel slices following SDS-PAGE.

Liquid Chromatography mass spectrometry (LC-MS)

Complexes obtained after the cross-linking step were loaded onto a 4–20% polyacrylamide gradient gels and Coomassie stained. The bands containing the complexes were cut and submitted to tryptic digestion.[35] The experiments were performed in duplicates for the 3 complexes D1:AVBS1-2, D1D2: AVBS1-2 and D1D2:AVBS1-3. Peptides obtained after tryptic digestion were analyzed on a Q Exactive Plus instrument (Thermo Fisher Scientific, Bremen) coupled with an EASY nLC 1 000 chromatography system (Thermo Fisher Scientific, Bremen). Sample was loaded on an in-house packed 50 cm nano-HPLC column (75 μm inner diameter) with C18 resin (1.9 μm particles, 100 Å pore size, Reprosil-Pur Basic C18-HD resin, Dr. Maisch GmbH, Ammerbuch-Entringen, Germany) and equilibrated in 98% solvent A (H2O, 0.1% FA) and 2% solvent B (ACN, 0.1% FA). A 120 min-gradient of solvent B at 250 nL.min-1 flow rate was applied to separate peptides. The instrument method for the Q Exactive Plus was set up in DDA mode (Data Dependent Acquisition). After a survey scan in the Orbitrap (resolution 70 000), the 10 most intense precursor ions were selected for HCD fragmentation with a normalized collision energy set up to 28. Charge state screening was enabled, and precursors with unknown charge state or a charge state of 1 and >7 were excluded. Dynamic exclusion was enabled for 35 or 45 s respectively.

Analysis of disulfide bridge by PEG-Maleimide modification

The determination of disulfide bridge formation in HV-CC was performed as previously described with minor modifications.[36,37] Briefly, for *in vitro* determination, 2 μg of purified HV or HV-CC were first incubated with 50 mM NEM PEG-Mal, NEM (N-ethylmaleimide), prior to reduction by incubation in 50 mM DTT (dithiothreitol). Alternatively, control samples were first reduced by incubation in 50 mM DTT, prior to NEM treatment. All samples were then incubated in 8 mM PEG-Mal (Sigma Aldrich, 63187). All incubation steps were carried out for 40 min at 21°C in 150 mM Tris pH 6.8, 0, 1% SDS (incubation buffer). Samples were precipitated and washed twice with acetone prior to resuspension between incubation steps. For determination of disulfide bridge formation in cells, HeLa cells were transfected with plasmids pC1-HV8His or pC1HV-CC8His the day preceding the experiment. Cells were scraped in 200 μls of ice-cold incubation buffer containing 1 mM AEBSF (4-(2-aminoethyl)benzenesulfonyl fluoride). Cell lysates were transferred to Eppendorf tubes on ice, 1800 uls of 150 mM Tris pH 6.8 containing 1 mM DTT (wash buffer) were added, and samples were clarified by centrifugation for 10 min at 13,000 g at 4°C. Clarified lysates were transferred to a fresh Eppendorf tube and subjected to pull-down by incubation with 40 μls of Ni Sepharose 6 Fast flow resin (Sigma Aldrich Pharmaceuticals) for 40 min at 4°C using an end-over-end roller. Samples were washed three times with 500 μls wash buffer. Samples were then subjected to NEM and DTT treatment prior to PEG-Mal modification as described above for purified proteins. Samples were resuspended in Laemmli loading sample buffer and SDS-PAGE analysis using a 7.5% polyacrylamide gel. For purified proteins, gels were analyzed by Coomassie blue staining. For proteins pulled-down from cell lysates, samples were analyzed by anti-vinculin Western blot analysis using the Vin11.5 mouse monoclonal antibody (Sigma Aldrich Pharmaceuticals) at a 1:5000 dilution.

Actin sedimentation assays

Actin was purified from rabbit muscle as described previously.[38] For actin co-sedimentation assays 5 μM actin was incubated in F-actin buffer (2 mM Tris pH7.5, 0.2 mM $CaCl_2$, 0.5 mM beta-mercaptoethanol, 0.2 mM ATP, 100 mM KCl, 2 mM $MgCl_2$) for 60 min at 21°C. When indicated, HV, HV-CC, AVBS1-3 and AVBS1-2 were added at a 2 μM final concentration. Samples were centrifuged at 110,000 g for 30 min at 4°C. For actin bundling assays, actin was allowed to polymerize at the indicated concentration and samples were centrifuged at 14,000 g for 10 min at 31°C. Proteins in pellets and supernatants were analyzed by SDS-PAGE on a 10% polyacrylamide gel followed by Coomassie blue staining. For quantification, protein band integrated densities were determined using ImageJ. The percentage of pelleted protein is calculated relative to the total amounts of the corresponding protein in the supernatant and pellet.

Fluorescent microscopy analysis of actin bundling by vinculin oligomers

HV and HV-CC were labeled using BodipyTM FL NHS Ester (Succinimidyl Ester) (ThermoFisher, D2184) following the manufacturer's instruction. Actin was fluorescently labeled with Alexa Fluor 594 Succinimidyl Ester as previously described.[38] To immobilize protein on beads, 30 μls of 1 μm-diameter red Fluorospheres (Molecular Probes, F8887) were incubated with 2 μM GST-AVBS1-3, GST-AVBS1-2 or GST as a control in 200 μL PBS for 120 min with end-over-end rolling at 4°C. Beads were washed three-times by successive centrifugation for 2 min at 14,000 g and resuspension in 200 μL PBS. 100 nm-diameter red Fluorospheres were coated with 2 μM of talin H1-H4[39] using a similar procedure. For each sample, 30 μL of the coated-bead suspension were centrifuged 2 min at 14,000 g, the supernatant was discarded and pelleted beads were resuspended in F-actin buffer containing 3.5 μM actin, 1.5 μM Alexa Fluor 594 -labeled actin, and HV or HV-CC at 1 μM final concentration in a total volume of 10 μL. Samples were incubated for 15 min at 21°C, Phalloidin Alexa Fluor 594 (Thermofisher, A12831) was added at a final concentration of 100 nM and incubation was allowed to proceed for another 45 min. Samples were mixed with DAKO mounting medium (DAKO, S3023), placed on a slide and covered by a 22 × 22 mm coverslip. Samples were analyzed using a Leica SP8 confocal microscope using a 63× oil immersion objective, at an image resolution of 2048× 2048, zoom 4.

Data analysis

The identification of cross-linked peptides from LC-MS data was performed using SIM-XL v. 1.3,[40] with the following search parameters: EDC as cross-linker, a tolerance of 20 ppm for precursor and fragment ions, trypsin fully specific digestion with up to three missed cleavages. Carbamidomethylation of cysteines was considered as a fixed modification. All initial identification of cross-linked peptides required a primary score of SIM-XL greater than 2.5 for inter-links and 2.0 for intra-links or loop-links. As single incorrect cross-link identification might lead to a different model, a manual post-validation of the search engine results at the MS2 level was thus performed. A 2D-map showing the protein-protein interaction was generated as an output. Only peptides present in the 2 replicates are gathered in Tables S1–S3 and were used for the modeling.

Modeling

We used the distance constraints obtained from cross-linking MS data (Tables S1–S3) to guide the protein structure modeling using the TX-MS protocol as described by Hauri et al., 2019.[21] In short, TX-MS uses the Rosetta comparative modeling protocol (RosettaCM),[32] and the flexible backbone docking protocol (RosettaDock)[33] to generate models and evaluate how well each model explains the MS constraints using a scoring function. Here, a total of 100,000 models was generated, of which the highest-scoring model is displayed in (Figure 3C), supported by a total of 100 inter and intra-molecular cross-links.

TIRF (total internal reflection microscopy) analysis

C2.7 cells were transfected with pmCherry-vinculin or pmCherry-VASP and the indicated plasmids as described above. Samples were mounted onto a TIRF microscopy chamber on a stage of an Eclipse Ti inverted microscope (Nikon) equipped with an Apo TIRF 100 x N.A. 1.49 oil objective heated at 37°C. TIRF analysis was performed using the Roper ILAS module and an Evolve EM-CCD camera (Roper Scientific Instruments). When mentioned, Y-27632 was used at 100 μM. Image acquisition was performed every 12.5 s for 30 to 90 min.

Invasion assays

Tissue culture Transwell inserts (8 μm pore size; Falcon, Franklin Lakes, NJ) were coated for 3 h with 10 μg of Matrigel following the manufacturer's instructions (Biocoat, BD Biosciences, San Jose, CA). Inserts were placed into 24-well dishes containing 500 μL of RPMI medium supplemented with 1% fetal calf serum. 5 × 10^4 melanoma cells were added to the upper chamber in 250 μL of serum-free RPMI medium. After 24 h, transmigrated cells were scored by bright field microscopy. Experiments were performed at least three times, each with duplicate samples.

QUANTIFICATION AND STATISTICAL ANALYSIS

Vinculin clusters induced by AVBS1-2- and AVBS1-3-coated beads were analyzed using the ImageJ 2.1.0/1.53c software. Briefly, for each set of experiments, sum projection images of confocal planes were thresholded using identical parameters between samples. Clusters were detected using the "Analyze particle" plug-in, setting a minimal size of 570 nm^2 and a maximal size of 120 000 nm^2. The vinculin cluster integrated fluorescence density was arbitrarily expressed as the percent of the mean integrated fluorescence density determined for vinculin clusters induced by AVBS1-2-coated beads (Figure 5).

Quantification of vinculin recruitment at the close vicinity of invading bacteria was performed on the sum projection of confocal planes corresponding to *Shigella*-induced actin foci. ROIs were drawn to delineate the actin foci (F) and the bacterial body (b) from the corresponding wavelength channel as shown in Figure S1. The vinculin recruitment index was calculated as the ratio of the average fluorescence intensity corresponding to vinculin labeling associated with (b) corrected to background over that of (F). For the quantification of the number and size of large adhesion structures induced by *Shigella* invasion in HeLa cells, the confocal fluorescent microscopy plane corresponding to the vinculin-labeled cell basal plane was processed using the ImageJ FFT/Bandpass followed by particle analysis plugins with a low size threshold set at 3.54 $μm^2$. A semi-automated protocol using Icy software was

developed for the quantification of adhesion structures in C2.7 cells.[31] Confocal fluorescent microscopy planes were used to detect vinculin structures using HK means thresholding and overlaid binary masks obtained from the threshold projections of F-actin labeled images (Max-entropy method). FAs were detected as spots positive for both vinculin mCherry and actin structures using Wavelet Spot Detector. The number of adhesions was analyzed using Dunn's multiple comparisons test. The statistical analysis of cell motility was performed in the R software. Medians were compared using a Wilcoxon rank-sum test and dispersion by Median absolute dispersion (MAD) parameter.